Title:

Spatial and molecular anatomy of germ layers in the gastrulating Cynomolgus monkey embryo

Guizhong Cui[1,7], Su Feng[1,7], Yaping Yan[2,7], Li Wang[3], Xiechao He[4], Xi Li[2], Yanchao Duan[2], Jun Chen[5], Patrick P.L. Tam[6], Ke Tang[5], Ping Zheng[4], Wei Si[2,*], Naihe Jing[1,3,*], Guangdun Peng[1,3,8,*]

[1]Bioland Laboratory (Guangzhou Regenerative Medicine and Health Guangdong Laboratory), Guangzhou 510005, China

[2]Yunnan Key Laboratory of Primate Biomedical Research, Institute of Primate Translational Medicine, Kunming University of Science and Technology, Kunming, Yunnan, 650500, China

[3]Ceter for Cell Lineage and Development, CAS Key Laboratory of Regenerative Biology, Guangdong Provincial Key Laboratory of Stem Cell and Regenerative Medicine, Guangzhou Institutes of Biomedicine and Health, Chinese Academy of Sciences, University of Chinese Academy of Sciences, Guangzhou 510530, China

[4]State Key Laboratory of Genetic Resources and Evolution and Yunnan Key Laboratory of Animal Reproduction, Kunming Institute of Zoology, Chinese Academy of Sciences, Kunming 650223

[5]Precise Genome Engineering Center, School of Life Sciences, Guangzhou University, Guangzhou, Guangdong 510006, China

[6]Embryology Research Unit, Children's Medical Research Institute, School of Medical Sciences, Faculty of Medicine and Health, University of Sydney, Westmead, New South Wales, Australia

[7]These authors contributed equally

[8]Lead contact

*Correspondence: siw@lpbr.cn (W.S.), jing_naihe@grmh-gdl.cn (N.J.), peng_guangdun@gibh.ac.cn (G.P.)

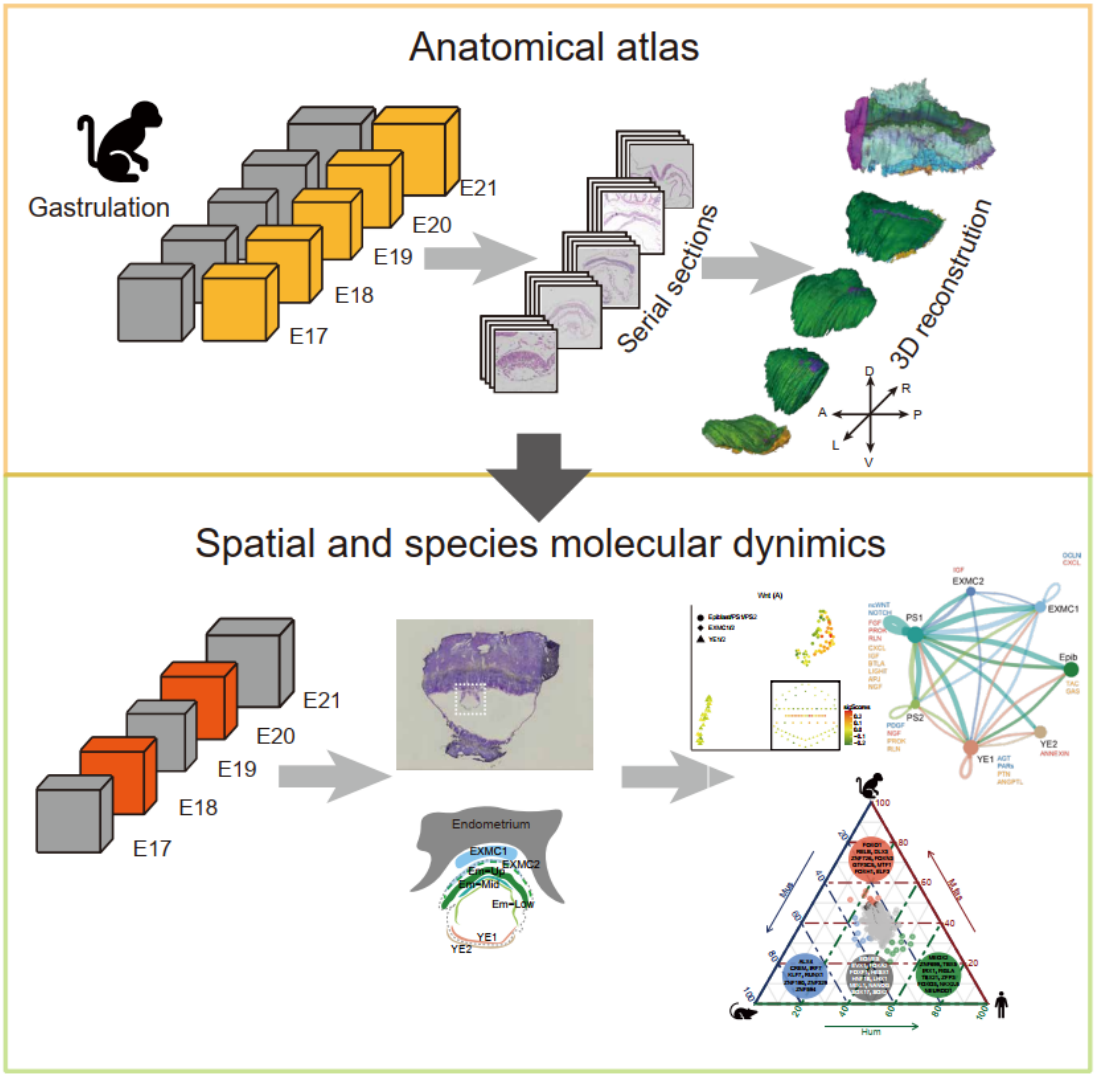

Highlight:

- A high-resolution anatomical atlas of Cynomolgus gastrulation embryos
- Created a three-dimensional digital template from serial sections of five developmental stages
- A two-dimensional spatiotemporal transcriptome of the germ layers of gastrulating embryos
- Cross-species comparison infers conservation of functional attributes of regulome and signaling activity in germ layer formation

Summary:

During mammalian embryogenesis, spatial regulation of gene expression and cell signaling are functionally coupled with lineage specification, patterning of tissue progenitors and germ layer morphogenesis. While the mouse model has been instrumental for our understanding of mammalian development, comparatively little is known about human and non-human primate gastrulation due to the restriction of both technical and ethical issues. Here, we present a morphological and molecular survey of spatiotemporal dynamics of cell types populating the non-human primate embryos during gastrulation. We performed serial sections of Cynomolgus monkeys (*Macaca fascicularis*) gastrulating embryos at 1-day temporal resolution from E17 to E21, and reconstructed three-dimensional digital models based on high-resolution anatomical atlas that revealed the dynamic changes in the geography of the mesoderm and primitive streaks. Spatial transcriptomics identified unique gene profiles that correspond to distinct germ layers and cross-species spatiotemporal transcriptome analysis revealed a developmental coordinate of germ layer segregation between mouse and primate. Furthermore, we identified species-specific transcription programs during gastrulation. These results offer important insights into evolutionarily conserved and divergent processes during mammalian gastrulation.

Key words

Germ layers, Gastrulation, Monkey embryo, Tissue lineages, Morphology, Spatial transcriptome, Cross-species analysis

Introduction

Gastrulation is fundamental for mammalian embryogenesis at which the definitive germ layers are established and the embryonic cell lineages are allocated to the basic body plan. During germ layer formation, cells undergo ordered changes in shape and fate under a spatiotemporally coordinated regulation. The anatomy of gastrulation has been studied in a variety of mammal species, including the mouse, human and nonhuman primate (Enders et al., 1986; Grobstein, 1985; Mittnenzweig et al., 2021; Moore et al., 1985; Nakamura et al., 2016; Pfister et al., 2007; Snow, 1977; Tarara et al., 1987; Tyser et al., 2020; Yang et al., 2021). In human embryos, the embryonic period is divided into 23 distinct morphological stages known as Carnegie stages (CS) (O'Rahilly and Muller, 2010). At the early CS6 stage (approximately 14 days post-fertilization, Embryonic day 14, E14), the posterior side of the pluripotent epiblast cells start gastrulating to generate three germ layer cells: the ectoderm, mesoderm, and endoderm. However, due to the limitation of the scope of experimental studies of human development up to the onset of gastrulation (Hyun et al., 2021) and the accessibility of embryonic samples, the developmental biology of the gastrulating human embryos is not known in detail.

Previous works have described the gastrulation of non-human primates in the context of morphogenesis and transcriptome, based on a few tissue sections and in vitro models (Hendrickx, 1972; Luckett, 1978; Ma et al., 2019; Nakamura et al., 2016; Niu et al., 2019; Tyser et al., 2020; Yang et al., 2021). However, little is known about the three-dimensional (3D) structure and the molecular landscape, such as the spatiotemporal pattern of gene expression, of gastrulating embryos, both of which are crucial for gaining structural insights of physiology and illustrating fate mapping. Importantly, in light of the kindled

93 interest of in vitro development of human and monkey early post-implantation
94 embryo and the stem-cell based embryo models (Fu et al., 2020; Moris et al.,
95 2020; Niu et al., 2019; Xiang et al., 2019; Zheng et al., 2019), it is imperative to
96 gain the knowledge of in vivo benchmarks of post-implantation development
97 particularly at gastrulation for use as a reference framework for interpreting the
98 outcome of in vitro modeling research. Therefore, high-resolution
99 morphological and spatial transcriptomic analysis of macaque gastrulating
100 embryos is an imperative scientific endeavour.
101
102 With the advent of single-cell RNA sequencing, the molecular phenotype of cell
103 types and their developmental trajectory in early mammalian development have
104 been unraveled (Nakamura et al., 2016; Peng et al., 2020b; Pijuan-Sala et al.,
105 2018; Tam and Ho, 2020; Tyser et al., 2020). However, the datasets of single-
106 cell molecular signatures are missing the spatial/positional information of the
107 cells of interest in embryo (Larsson et al., 2021; Peng et al., 2020a). Our
108 previous work showed that spatially resolved transcriptome, not only generates
109 a 3D digital “in situ hybridization” gene expression dataset for mouse
110 gastrulation, also enables the reconstruction of the molecular trajectory of cell
111 populations at gastrulation in time and space (Peng et al., 2019). As the
112 morphogenetic program of immediate post-implantation development of the
113 embryo is different between the mouse and the human, it is far from certain that
114 the rodent-specific developmental mechanism can be extrapolated to the
115 human embryo. It is a widely held view that non-human primate is the more
116 appropriate model for human embryo development (Nakamura et al., 2021).
117 However, systematic profiling of spatial transcriptome in gastrulating monkey
118 embryos has yet to be accomplished, albeit single-cell transcriptome has been
119 documented for Cynomolgus monkey embryo at E6- E17, which did not extend
120 to the gastrulation stages. Here we performed Geo-seq (Chen et al., 2017) to

121 interrogate the molecular architecture and lineage commitment of the
122 Cynomolgus monkey gastrulation embryos. We first established a high-
123 resolution anatomical atlas to describe the key morphogenetic processes and
124 three-dimensional topographical change during three germ layers formation of
125 Cynomolgus monkey embryo. We then established a molecular atlas depicting
126 the spatial pattern of gene expression at two timepoints (E18 and E20) of
127 gastrulation. Finally, we undertook cross-species comparative analysis of
128 spatiotemporal transcriptome data of mouse, Cynomolgus monkey and human
129 embryos to identify molecular programs that may underpin the evolutional
130 convergence, as well as divergence, of the developmental mechanism of
131 gastrulation across these species. Our atlas can be explored via the interactive
132 website.
133

134 Results

135 Structural characteristics of gastrulating embryos in non-
136 human primate

137 Cynomolgus monkey (*Macaca fascicularis*) gastrulating embryos (E17, E18,
138 E19, E20 and E21, equivalent of carnegie stage 6-9) were isolated after in vitro
139 fertilization (IVF) procedure with ethical approval (STAR Methods, Figure 1A-E
140 and S1A-C). The embryos were staged by calculating the gestation days aided
141 by transabdominal ultrasound monitoring. At least two embryo replicates at
142 each developmental stage were studied (Figure S1C) with a very good
143 consistence (Figure 1A-D, S1D-E and Figure S7G). Having the complete
144 representation of embryos of gastrulation stages allow us to build a holistic view
145 of tissue morphogenesis for non-human primates.

146

147 Corroborating previous observations on human and rhesus embryos (Enders
148 et al., 1986; Ghimire et al., 2021; Grobstein, 1985; Luckett, 1978; Nakamura et
149 al., 2016), post-implantation Cynomolgus embryos acquired a disc-like
150 configuration and are located on the center of the dome-shaped implantation
151 site which protrudes above the endometrial surface (Figure 1A-E). The
152 extraembryonic mesenchyme has invaded the primary villi to form the
153 secondary villi at E17 (Figure 1A and A', black arrow). At the tips of secondary
154 villi, cytotrophoblast (CT) cell converged into a thick cytotrophoblastic sheath
155 interspersed with syncytiotrophoblast (ST). Rodent extraembryonic mesoderm
156 originates from the epiblast during gastrulation, whereas the developmental
157 origin of primate extraembryonic mesoderm is hypothesized mainly from the
158 hypoblast-derived primary yolk sac (Bianchi et al., 1993; Ross and Boroviak,
159 2020). Remarkably, we found that in contrast to mouse, extraembryonic
160 mesoderm of primate embryos was formed before the onset of gastrulation
161 (Figure 1A'). As previously reported, the primate extraembryonic mesoderm
162 constituted the tissues that support the epithelium of the amnion and yolk sac
163 and the chorionic villi (Figure 1A'-E') (Carlson, 2015). Additionally, the
164 extraembryonic mesoderm splits into two layers, extraembryonic somatic
165 mesoderm (EXSOM) lining the amnion and extraembryonic splanchnic
166 mesoderm (EXSPM) lining the yolk sac (Figure 1A'-E'). These extraembryonic
167 mesoderm cells were subsequently merged with primitive streak (PS)-derived
168 extraembryonic mesoderm to establish the connecting stalk (embryonic stalk),
169 which attaches the whole conceptus to the chorion (Figure 1A' and Figure S2-
170 6)(Enders and King, 1988). Of note, a unique feature of primate embryos is the
171 formation of secondary yolk sac (SYS) on the hypoblast side the embryonic
172 disc (ED), consisted of an expanding hypoblast (HYP) and squamous yolk sac
173 parietal endoderm (YSPE), gradually expand following gastrulating (Figure 1A'-

174 E'). In the opposite side of ED, amniotic cavity (AC), consisting of a fluid-filled
175 sac surrounding the embryo, was enclosed by low cuboidal epithelium shaped
176 amnion (AM) with epiblast cells.
177
178 The formation of the primitive streak (PS) in the midline of the embryonic disc
179 heralds the onset of gastrulation. The epiblast (EPI) was pseudostratified with
180 the properties of typical epithelial cells, and with the elongation of the PS,
181 epiblast cells undergo epithelial-to-mesenchymal transition (EMT) to ingress
182 toward the space between the epiblast and hypoblast, generating mesoderm
183 (ME) wings (Figure 1A'-D'). The anterior-posterior length of epiblast increases
184 from 200μm at early gastrulation (E17) to 900μm at late gastrulation (E20)
185 (Figure 1F and Table S1). The primitive streak spans 20% of the anterior-
186 posterior length of the embryonic disc at E17, increasing to 40% by E20 (Figure
187 S1J). The PS gradually extends to the anterior epiblast, marking a progress of
188 gastrulation (Ghimire et al., 2021; Muller and O'Rahilly, 2004).
189

190 Cell number and cell cycle kinetics of primate gastrulating 191 embryos

192 A remarkable feature of the development of gastrulating embryos is the
193 regulation of cell growth, especially the mitotic division that results in the
194 increase in cell numbers. In mouse, the embryo that lack normal numbers of
195 cells due to the disruption of cell proliferation or cell death will delay gastrulation
196 until the appropriate number of epiblast cells has been attained (Snow, 1977;
197 Tam and Behringer, 1997). However, the number of cells of the primate embryo
198 during gastrulation remains to be investigated. We obtained a near complete
199 collection of tissue sections, therefore we applied detailed histological analyses
200 on serial sections to determine the kinetics of cell division (STAR Methods,

Figure 1G and S1F-I, Table S2). At E17, the early stage of primate gastrulation, the epiblast was about 850 cells, and the hypoblast was approximately 370 cells (Figure 1G and S1K). Subsequently, the number of cells in gastrulating embryos increased rapidly. By the end of gastrulation, the whole embryo was about 9100 cells (4500 cells in the ectoderm, 2200 cells in the mesoderm, and 2300 cells in the endoderm) (Figure 1G and S1K). Analysis of growth rate by determining cell number increase, and by mapping mitotic activity in the germ layers showed that the cell generation time for epithelial ectoderm and endoderm was estimated at about 27 hours (Figure S1K). Notably, the average cell generation time of the mesoderm, perhaps caused by the migration of epiblast and the proliferation of nascent mesoderm, was significantly shortened to 16 hours (Figure S1K). Given that the primitive streak covered about 1/5 of the epiblast at E17 (Figure S1J), the initiation of gastrulation in Cynomolgus monkey embryo was estimated to be approximately at E16 (Nakamura et al., 2021; Nakamura et al., 2016). To assess the threshold number of epiblast cells which is critical for the initiation of gastrulation, the epiblast and hypoblast at starting gastrulation were calculated about 490 and 200 cells, respectively, based on the kinetics of cell proliferation in macaque embryo. Interestingly, the mean cell generation time during primate gastrulation was the half of pre-gastrulation, which is consistent with the pattern found in mouse (Figure S1L) (Snow, 1977). In addition, the length of epiblast progressively increases and the size of the embryo becomes larger (Figure 1F, Table S1). That is slightly different from the in vitro culture system (Niu et al., 2019). Both in vivo and in vitro embryos have similar same size at the early stage of gastrulation, but subsequently, natural embryos become larger while cultured embryos do not change too much in size. This discrepancy may be due to the limitation of the in vitro culture system for complex structural development.

Cellular anatomy of primate gastrulation embryo

Morphogenetic movements including cell migration and reorganization during gastrulation reshape the embryos. A paramount event is the epithelial to mesenchymal transition (EMT). EMT involves changes of epiblast cells from a proper epithelium with the full array of epithelial characteristics to mesenchymal-shaped mesoderm cells (Massri et al., 2021). During the initiation of mouse gastrulation, the PS, a transient embryonic structure where gastrulation EMT took place, was formed at the posterior of the epiblast. We observed that EMT follows similar patterns in monkey embryos (Figure 2 G-H and G'-H', white open arrowheads). The epiblast cells were contiguous with amnion cells at the margin of the disc, where there was a gradation in cell size from columnar to low cuboidal spanning two to three cells (Figure 2 E-F and E'-F', asterisks). Cells that remain in the epiblast are allocated to the ectoderm (ECT) (Ghimire et al., 2021; Shahbazi, 2020). A thick basement membrane lining the epiblast surface was visible in the anterior region (Figure 2 A-C and A'-C', black arrows), while epiblast cells in the primitive streak were still connected to the rest of the epiblast with the onset of gastrulation (Figure 2 G-H and G'-H', white open arrowheads). These cells changed their shape from tall column to triangle, lost the epiblast cell–basement membrane interaction, and were squeezed together. During gastrulation, we found that cells ingress through the PS, break down the basement membrane, and invade into the space between the hypoblast and epiblast to form the intraembryonic mesoderm (Figure 2 E-H and E'-H', black open arrowheads). There were also cells that migrated posterolaterally beyond the embryonic disc border to form extraembryonic mesoderm (Figure 2 F-H and F'-H', white arrows). Thus, the epiblast undergoes a drastic morphological transition, engaging intra/extraembryonic mesoderm cells into a migratory behavior.

256

257 Notably, some gastrulating cells posterior to the leading edge of the mesoderm
258 wrings were found to undergo mesenchymal epithelial transition (MET), the
259 reverse mechanism of EMT, as they intercalate into the overlying hypoblast
260 (visceral endoderm) epithelium to form the gut endoderm on the surface of the
261 embryo (Figure 2 E'-G', K'-L' and Figure 3 C'-E',K'-M', black arrowheads).
262 These MET cells, with obvious mesenchymal characteristics, were larger than
263 the pre-existed hypoblast cells but were not in a dominative presence. As
264 previously reported that there were two populations of definitive endoderm cells
265 in human gastrulation embryos by single cell transcriptome analysis (Tyser et
266 al., 2020), this may suggest that the mixing of these two (embryonic and
267 extraembryonic) endodermal populations collectively comprises the definitive
268 gut endoderm, as they do in the mouse embryo (Viotti et al., 2014).

269

270 Next, to address the intricate morphogenesis of the developing primate embryo,
271 the three-dimensional (3D) anatomical atlas was performed based on serial
272 sections with the collected gastrulation embryos. In line with knowledge from
273 3D reconstruction of human specimen, we found that the epiblast of
274 Cynomolgus monkey changed from a globe-like into a disc-like shape, with the
275 primitive streak in the midline (Figure 2N-O and Figure 3K, P). Afterwards, the
276 flat disc shape was distorted as the embryonic cavity increases and perfect
277 morphology is difficult to be preserved without perfusion (Figure 3 O, P and S5).
278 At the end of gastrulation, the embryo which begins as a flat sheet of cells, folds
279 to acquire a typical cylindrical shape (Figure 4 and S6). The ectoderm
280 developed into neural ectoderm and surface ectoderm, then neural ectoderm
281 underwent bending to create the neural folds, which converge towards the
282 dorsal midline (Figure 4 A-C and E) (Nikolopoulou et al., 2017). The mesoderm
283 continually developed in the tail bud (Figure 4 D), and divided into the paraxial

284 mesoderm, intermediate mesoderm, and lateral plate mesoderm (Figure 4 C)
285 (Tani et al., 2020). The paraxial mesoderm gives rise to the somite, a notable
286 feature of early organogenesis, mainly through somitogenesis (Lawson and
287 Wilson, 2016). Besides, somite count is a convenient means to stage embryos,
288 and there were 5 or 6 somites visible at E21, corresponding to CS9 of human
289 embryo development (Figure 4 C and E). After gastrulation, the gut endoderm
290 was regionalized along the dorsal-ventral (D-V) and anterior-posterior (A-P)
291 axes into broad foregut, midgut, and hindgut domains. In the monkey embryos,
292 we observed that the foregut pocket invaginated to generate the anterior
293 intestinal portal, while the hindgut pocket at the posterior formed the caudal
294 intestinal portal, a process similar to that in the mouse embryo development
295 (Figure 4 E and S6) (Nowotschin et al., 2019). Together, we reconstructed the
296 histologic detail based on more than 100 serial high-quality sections and
297 provided a digitalized anatomy atlas for the Cynomolgus gastrulation monkeys
298 which can serve as valuable reference for primate embryogenesis.
299

300 Molecular architecture of the gastrulating monkey embryo

301 Previously, we conducted a spatiotemporal transcriptome on the mouse embryo
302 by low-input Geo-seq during gastrulation from E5.5 to E7.5 stages (Peng et al.,
303 2019). To achieve a spatial molecular profiling of primate embryos during
304 gastrulation, we applied Geo-seq to analyze the expression of genes in
305 embryonic and extraembryonic tissues at E18 and E20 (Figure 5A and S7A-C,
306 STAR Methods). Although the tissue morphology of cryo-sections was inferior
307 to paraffin embedding sections, the germ layers were discernable. We divided
308 the embryonic tissues into the upper, middle and lower layer (Em-Up, Em-Mid
309 and Em-Low) according to the dorsal-ventral axis based on the anatomical
310 structure. Furthermore, extra-embryonic mesenchyme 1 and 2 (EXMC1/

311 EXMC2) and yolk-sac parietal endoderm (YE1) and extraembryonic
312 mesemchyme lining the yolk sac (YE2) were captured from extraembryonic
313 tissues according to their locations in the amniotic cavity and secondary yolk
314 sac (Figure S7A-C). The spatial transcriptome of primate gastrulating embryos
315 provides a high- depth and quality dataset, with ~15M mapped reads, ~87%
316 mapping ratio, and 12,000 genes on average (Figure S7F). The consistency
317 between two replicates or developmental stages was more than 0.94, indicating
318 we can rely on these data to probe the molecular architecture of the primate
319 embryo (Figure S7F). We further generated a dot plot to facilitate the planar
320 (top represents dorsal and bottom represents ventral) display of the spatial
321 expression of the combined gastrulating primate embryos, which called STGE-
322 plot (Spatial Transcriptome of Gastrulating Embryos), according to the
323 geography and morphology of qualified samples (n=86) (Figure 5A).
324
325 Next, we performed principal component analysis (PCA) and uniform manifold
326 approximation and projection (UMAP) of the tissue samples with unsupervised
327 clustering, and the result showed tight clustering of samples by spatial positions
328 (Figure 5B), pointing to a location-dependent germ layer specification. To
329 characterize the functional status of gene regulatory network (GRN), we
330 performed SCENIC (single-cell regulatory network inference and clustering)
331 (Aibar et al., 2017) analysis (STAR Methods). The specifically enriched regulon
332 activity based on transcription factors and their co-expressed target genes was
333 further grouped into 11 modules that are specifically activated in seven spatial
334 cell clusters (Figure 5 C and E). In line with the unsupervised clustering of
335 transcriptome, the regulon-based dimensionality reduction showed that the
336 tissue type and spatial location were clearly delineated on the top three PC
337 axes (Figure 5C). The PC1 axis defined cell types of embryonic and extra-
338 embryonic tissues, and the PC2 and PC3 axis represented the spatial variances.

339 Therefore, the signatures of tissue types and geographical regions of
340 Cynomolgus monkey gastrulating embryos were distinguished by both gene
341 expression and regulatory activity.
342
343 To investigate the lineage identities of spatial samples, we incorporated key
344 marker genes, regulon activities, geographical anatomy and cell-type
345 deconvolution to infer spatial molecular organization of primate gastrulation.
346 For cell-type deconvolution in spatial transcriptome, SPOTlight that based on a
347 non-negative matrix factorization (NMF) regression algorithm was used to infer
348 the location of cell types (Elosua-Bayes et al., 2021). We integrated both in vivo
349 single cells (Nakamura et al., 2016) and our spatial transcriptomics data of
350 monkey gastrulating embryo, and demonstrated that gastrulating cells (Gast1,
351 2a and 2b) were mainly located in middle and lower layer of embryonic disk
352 whereas the post-implantation late epiblast cell (PostL.EPI) account for the
353 largest proportion in the upper layer of embryo (Figure S7D). In line with cell-
354 type deconvolution analysis, the correlation coefficiency of gene expression
355 showed that the upper layer of embryonic tissues was more similar to the
356 epiblast cells, whereas there was a discrete regional property of embryonic and
357 extra-embryonic cell types (Figure S7E). In addition, the spatially captured
358 tissue from gastrulating monkey embryos were consistent with cells of human
359 CS7 gastrula (Figure 5D). Human epiblast like cells mainly located in Em-Up,
360 primitive streak cells were including in Em-Mid, while extra-embryonic
361 endoderm cells were separated into Em-Low, YE1 and YE2.
362
363 We identified marker genes and regulatory networks that are critical for the
364 molecular annotation of the spatial samples and found there is a considerable
365 conservation between species. For example, the *POU5F1*, *HESX1*, *SOX2* and
366 *NANOG* pluripotency regulatory network were highly activated in embryonic

367 tissues, particularly in the upper layer which are epiblast and its derivatives
368 (Figure 5E), corroborating previous findings (Boroviak et al., 2018) (Nakamura
369 et al., 2016; Niu et al., 2019; Xiang et al., 2019) (Figure S7J and K). Notably, in
370 contrast to that in the rodent model, *NANOG* and *PRDM14* were still highly
371 expressed in the embryonic tissues until the middle and late stages of
372 gastrulation in primate, suggesting a distinct spectrum of pluripotency during
373 gastrulation.
374
375 We found that the PS-related genes *TBXT*, *MIXL1* and *FOXA2* showed high
376 expression in the Em-Mid and Em-Low of the epiblast, but was low in the yolk
377 sac endoderm and extra-embryonic mesenchyme (Figure S7J). Similarly, the
378 G4 regulon, consisting of MIXL1, EOMES, FOXA2 and SOX17, were
379 specifically activated in the Em-Low and Em-Mid regions and were enriched
380 with terms such as “Endodermal cell differentiation” and “Regionalization”
381 (Figure 5E). In line with the anatomical annotation, spatial territory of epithelial
382 to mesenchymal transition (EMT) genes demonstrated that epiblast cells at this
383 region undergo an EMT during gastrulation (Figure S7K). Furthermore, the
384 activating activity of the WNT and NODAL signaling pathways were
385 predominantly enriched (Figure 5F and S7K). Em-Low and Em-Mid were
386 distinguished by their relative expression of G1 regulon which were enriched in
387 chromatin remodeling, such as SP1 and KDM4B, suggesting that epigenetics
388 has a pivotal role in lineage commitment (Nicetto et al., 2019; Wang et al., 2018).
389 Therefore, we classified the middle and lower layer of embryo into PS1 and
390 PS2, which may denote gastrulating cells of slightly different status.
391
392 Interestingly, the yolk-sac tissues (YE1 and YE2) showed the least similarity to
393 the other dissected regions, as revealed both by UMAP and hierarchical
394 clustering (Figure 5B and S7H). α-fetoprotein (*AFP*), transthyretin (*TTR*) and

395 albumin (*ALB*) were highly expressed in YE1 and YE2, and they also formed
396 co-expression module (Figure S7I and J). The expression of *AFP*, *TTR* and
397 *ALB* was usually regarded as the earliest marker of hepatoblasts (Gualdi et al.,
398 1996; Sheaffer and Kaestner, 2012), while the yolk sac may serves as a pivotal
399 organ for diverse functions of intestine, liver, bone marrow and thyroid even
400 before the matured organs have not been generated at the early embryo
401 development stages (Ross and Boroviak, 2020; Wong and Uni, 2021).
402 Additionally, the apolipoprotein gene family members were also specifically
403 expressed in yolk-sac endoderm, such as *APOA1* (Figure S7J), *APOA2/4* and
404 *APOC2/3* (from DEGs, data not show), which is consistent with the function of
405 the yolk sac as the primary site of apolipoprotein synthesis during early primate
406 and mouse development (Baardman et al., 2013; Cindrova-Davies et al., 2017).
407 Furthermore, as previously reported that primate yolk sac delivers nutrients and
408 oxygen to the embryo early in development (Cindrova-Davies et al., 2017; Dong
409 and Yang, 2018; Exalto, 1995), pathway activity analysis and weighted gene
410 co-expression network analysis (WGCNA) showed that reactome of oxygen
411 release and AMI pathway involving collagen (*COL4A1/2/3/4/5/6*), fibrinogen
412 (*FGA, FGB* and *FGG*) and serpin members (*SERPINC1*) were enriched
413 exclusively in the yolk sac tissues (Figure S7I and K). Notably, we identified
414 FOXA1, FOXA3 and NR1H4 as the key transcript factors in maintaining the
415 identities of yolk sac endoderm (Figure 5E and H) and have the most
416 connections within the regulon group and the node-regulons. Previously,
417 FOXA1 was defined as the visceral/yolk-sac endoderm (VE/YE) marker
418 (Nakamura et al., 2016), hence our analysis further indicated that FOXA1 and
419 FOXA3 correlate with yolk sac endoderm fate specification, whereas FOXA2
420 were functionally critical for mesoderm and definitive endoderm development
421 (Figure 5E and H).
422

423 Cellular fate specification depends on temporally and spatially precise cell
424 communication, so we performed intercellular communication analysis based
425 on ligands, receptors and their cofactors by CellChat (Jin et al., 2021). Although
426 not at single-cell resolution, the cell-cell communication network identified PS1
427 cells as the dominant communication “hub” (Figure 5G). PS1 cells were mainly
428 enriched with WNT and NOTCH signaling pathway in a paracrine and autocrine
429 manner (PS1 and PS2), which is consistent with their known roles (Figure 5G)
430 in gastrulation (Nakamura et al., 2016; Souilhol et al., 2015). In agreement with
431 previously work in mouse (Ciruna and Rossant, 2001; Sun et al., 1999), we
432 identified that PS1 was the primary FGF source in primate, signaling both in
433 autocrine and paracrine manner with FGF15 − FGFR1, FGF17 − FGFR3 and
434 FGF17 − FGFR1 ligand-receptor pairs to drive the migration of delaminated
435 cells and the differentiation of the mesendoderm.
436
437 To uncovered the key sequential signaling events along the process of primate
438 gastrulation, we combined the communication pattern analysis with the
439 previously studied cell events in mouse and human cell models. It’s known that
440 the BMP signaling in the extraembryonic ectoderm in mouse was the source of
441 signaling molecules that transduce the fate of proximal epiblast cells, which
442 formed the primitive streak subsequently (Ben-Haim et al., 2006; Brennan et al.,
443 2001; Chhabra et al., 2019; Rivera-Perez and Hadjantonakis, 2015; Rivera-
444 Perez and Magnuson, 2005). In contrast to mouse, primate embryos form the
445 extraembryonic mesoderm prior to gastrulation, and the BMP signaling was
446 highly enriched in the extraembryonic mesoderm (Figure S7K), suggesting that
447 the extraembryonic mesoderm may serve as a source of signaling molecules
448 in initiation of primate gastrulation. Notably, Hippo-Yap signaling was highly
449 activated in the extraembryonic mesoderm (Figure 5F). Previous work has
450 highlighted the Hippo signaling in regulating early endoderm development

451 during mouse gastrulation (Peng et al., 2019) and the crosstalk between TAZ
452 and SMAD (Varelas et al., 2008), therefore the co-localization of BMP and
453 Hippo/Yap signaling in the extraembryonic mesoderm may hint that Hippo-Yap
454 interacts with BMP signaling to initiate gastrulation of primate. Remarkably,
455 insulin-like growth factor (IGF) signaling was prominently secreted from EXMC2
456 cells to PS1 cells, and autocrine and paracrine loops of prokineticins (PROK)
457 were established between PS1 and PS2 in monkey gastrulating embryo (Figure
458 5G and S7L). IGF signaling pathway has been highly conserved and plays an
459 important role in early mesoderm formation of zebrafish and rabbits, which
460 influences the expression of *Otx2*, *FGF8*, *BMP2b*, *Wnt3a* and *Brachyury* (Eivers
461 et al., 2004; Thieme et al., 2012). In addition, IGF1 induced EMT process
462 through the activation of NFκB by the PI3K pathway, then induce SNAIL1
463 stabilization (Lamouille et al., 2014; Singh et al., 2018). Together, we predicted
464 that BMP, Hippo-Yap and IGF signaling pathway would be imperative to initiate
465 gastrulation in primate, and the communication pattern of CXCL, BTLA, LIGHT
466 and APJ is also from the EXMC to the PS1 specifically (Figure 5G).
467

468 Cellular and molecular dynamic of macaque gastrulation

469 To further confirm the observed characteristics of germ layer differentiation, the
470 expression of germ layer-specific molecular markers at RNA and protein levels
471 were investigated (Figure 6A and B). Consistent with previous reports, OCT4
472 (*POU5F1*) was exclusively expressed in the pluripotent cells, especially in the
473 epiblast and ectoderm of early or late gastrulation. GATA6 was specifically
474 detected in the hypoblast by immunohistochemical staining. Notably, we found
475 that the EMT cells were weakly positive for OCT4 and strongly express T, a
476 marker for primitive streak or nascent mesoderm. Interestingly, some
477 mesenchymal cells with the weak expression of T intercalated in the hypoblast

478 (Figure 6 B, white arrowheads), as shown in the histological images analyzed
479 previously (Figure 2 and 3), suggesting a prerequisite for downregulation of the
480 primitive streak genes in forming the definitive endoderm. Furthermore, spatial
481 gene expression showed that *NANOG* still marks pluripotent cells in the epiblast
482 (Figure 6 A and S7J). Taken together our three-dimensional gastrulating model
483 (Figure 6C) provides new insights for the molecular architecture of primate
484 gastrulation.
485

486 Cross-species spatiotemporal transcriptome analysis of 487 mammalian gastrulation development

488 Gastrulation is a fundamental morphogenetic process in development, and the
489 key signaling pathways that regulated the establishment of germ layers were
490 evolutionarily conserved, such as the role of WNT, NODAL and BMP signaling
491 pathways in non-human primate and rodent mammalians. However, there are
492 significant difference between primates and mice in both morphology and
493 development rate of gastrulation. To systematically reveal the molecular
494 signatures associated with different mammalian species, we performed cross-
495 species comparative analysis on the spatiotemporal transcriptome in mouse,
496 Cynomolgus monkeys and human gastruloid (STAR Methods). We showed that
497 the states of Cynomolgus monkey at E18 and E20 were resembling to the
498 middle-late stage of mouse gastrulation (Figure 7A and S8A). We aligned the
499 regulons along the developmental time and obtained 5 clusters that correspond
500 to the dynamic patterns of cell fate commitment and regionalization (Figure
501 S8B). All these dynamic regulons (n=451) across gastrulation were subjected
502 to dimensionality reduction analysis. The PCA plot showed that the cell types
503 between monkey and mouse were clustered together, suggesting a germ lay
504 consistency (Figure 7B). The PS1 and PS2 in macaque gastrulating embryos

505 were close to the mouse mesoderm and endoderm, respectively. To explore the
506 species-specific molecular mechanism underlying the germ layer segregation,
507 we defined a species/spatial domain-specificity score (SSS) based on Jensen-
508 Shannon divergence (STAR Methods). The activities of most regulons (more
509 than 50%) were similar during germ layer formation in mice and monkeys,
510 suggesting that the major gastrulation events are conserved and common
511 molecular regulatory mechanisms are shared between species (Figure 7C-E,
512 S8C-E, Table S3). Next, we looked into the species difference in germ layers
513 and whole embryonic tissues (Figure 7C-F). For quantitative visualization of
514 species specificity, relative SSS of regulons were plotted in ternary plot (Figure
515 7F). The activity of KLF7 were preferred in mouse, especially in the ectoderm
516 and the endoderm differentiation (Figure 7C, E and F), whereas the ELF3 were
517 enriched in the ectoderm of macaque (Figure 7C and F). Given that *Klf7* had
518 inhibitory activity on mesoderm (Gao et al., 2015) and *Elf3* was a negative
519 regulator of epithelial-mesenchymal transition in gastrulation and tumor
520 metastasis (Scheibner et al., 2021; Yeung et al., 2017), this might imply that
521 mice and non-human primates use functionally similar but different regulatory
522 factors in the maintenance of the ectoderm epithelium.
523
524 Interestingly, we found that Forkhead box transcription factor of subclass O
525 (FOXO) family showed species-dependent activity. Specifically, we showed that
526 FOXO1 was exclusively activated in macaque gastrulating embryos and mouse
527 embryos exhibited the highest levels of FOXO4 regulons, while FOXO3 activity
528 was substantially elevated in human (Figure 7G-H). In line with that FOXO1
529 regulates core pluripotency factors in human and mouse embryonic stem cells
530 by promoting the expression of *OCT4* and *SOX2* (Zhang et al., 2011), we found
531 that FOXO1 have a strong positive correlation with stem cell pluripotency genes
532 *SOX2* and *ZSCAN10*, which enriched in negative regulation of cell

533 differentiation and transcriptional regulation of pluripotent stem cells (Figure
534 S8F). Furthermore, we identified the targets of FOXO1/3/4 and their top related
535 genes. They also showed species differences with FOXOs expression,
536 including *TERT* (telomerase reverse transcriptase), *BCL6* and *TEF* (thyrotroph
537 embryonic factor) in mouse, macaque and human embryos respectively (Figure
538 S8H-J) (Chakravarti et al., 2021; Tang et al., 2002; Yamashita et al., 2014; Yang
539 et al., 2019). Together, our data indicate that FOXOs may play a vital role in
540 interspecies differences during gastrulation. Considering the prominent role of
541 FOXO family in metabolic homeostasis and organismal longevity, the species-
542 specific mechanisms may imply profound effect of FOXO in even beyond
543 embryo gastrulation.
544

545 # Discussion

546 In this study, we have provided an anatomical atlas and molecular database
547 spanning the entire gastrulation to the early organogenesis period of
548 Cynomolgus monkey development. This analysis was a critical step in
549 understanding of human embryology within similar time-window, which remain
550 largely unknown due to technical difficulties and ethical issues. First, we have
551 captured a series of high-resolution tissue anatomical sections from early
552 gastrulation (E17) to early organogenesis (E21), revealed the dynamic changes
553 of cell histomorphology and cell proliferation kinetics, and discovered the critical
554 role of cell migration and EMT/MET transformation in the process of germ layers
555 formation. Secondly, the three-dimensional model of primate embryos was
556 reconstructed to analyze the dynamics of gastrulation from a holistic
557 perspective. Furthermore, the spatial transcriptome of macaque gastrula has
558 been performed. We identified the key regulons and their interaction networks

559 in different cell types in the process of germ layer segregation. Finally, we have
560 explored cross-species differences in mouse, Cynomolgus monkeys and
561 human by comparatively analyzed the spatiotemporal transcriptomes.
562
563 Gastrulation is a period of rapid growth, proliferation and differentiation. Several
564 morphological and genetic reports in mouse have shown that the cell cycle
565 progression is coordinated with transcription, cell migration, and cell
566 differentiation (Abe et al., 2013; Mitiku and Baker, 2007; Snow, 1977; Tam and
567 Behringer, 1997), while little is known about this in primate gastrulation. We
568 have applied detailed histological analyses to assess the growth rate by
569 determining the cell number increase, and highlighted the cell proliferation
570 kinetics in primate gastrulation. However, the tissue- and embryo-wide division
571 patterns in primate gastrulating embryos needs further to be studied through
572 genetic markers labeling and spatial omics, because the rate of proliferation
573 differs significantly across the different regions of the epiblast in mouse at
574 gastrulation stages (McDole et al., 2018; Snow, 1977).
575
576 Although the morphology of primate embryonic development has been studied
577 for at least a century (de Bakker et al., 2016; Grobstein, 1985; Hendrickx, 1972;
578 Luckett, 1978), detailed anatomical imaging with high temporal resolution in
579 primate gastrulating embryos are lacking. We provided an atlas with sequential
580 stages and serial sections of gastrulating embryos in 2D and 3D, which was
581 fundamental to reveal cellular morphological changes during ectoderm,
582 mesoderm and endoderm formation. The results of this study showed that
583 mesenchymal like cells were found intercalated in hypoblast individually, not as
584 a coordinated sheet to displace the original hypoblast (Figure 2 and 3). And
585 immunohistochemical staining indicated that embedded mesenchymal cells
586 weakly expressed the primitive streak marker T (Figure 6B), implying that the

587 original hypoblastic cells could become integrated into the newly formed
588 embryonic endodermal layer and EMT/MET play important roles in the
589 embryogenesis of primate endoderm.
590
591 Remarkably, from the spatial transcriptome of monkey gastrulating embryos,
592 FOXA subfamily was found to have important biological functions in embryonic
593 and extraembryonic endoderm specification (Figure 5E and H). From the
594 evolution and phylogeny view, FOXA genes have a conserved role in the
595 development of the derivatives of the primitive gut (Hannenhalli and Kaestner,
596 2009; Lai et al., 1991), whereas the functional diversity among FOXA proteins
597 with the spatio-temporal expression patterns were not clear. In mouse, neither
598 *Foxa1* nor *Foxa3* inactivated mutants exhibit any early phenotype (Grapin-
599 Botton and Constam, 2007; Kaestner et al., 1998), whereas they can
600 compensate for the loss of *Foxa2* in the null mutants, which allows hindgut, but
601 not foregut and midgut formation (Dufort et al., 1998; Monaghan et al., 1993;
602 Sasaki and Hogan, 1993). In detail, the *FOXA1* was not just as the yolk-sac
603 endoderm marker (Nakamura et al., 2016), but also regulate yolk sac endoderm
604 fate specification with *FOXA3*. On the other hand, *FOXA2* had a pivotal role in
605 cell fate commitment of embryonic endoderm, which was consistent with the
606 finding in single cell transcriptome of human (Tyser et al., 2020). Indeed, the
607 molecular map of cell populations at defined positions varies. Our Geo-seq
608 approach may not be able to separate the mesoderm and endoderm cells at
609 single-cell resolution, therefore results in a relatively similarity at transcription
610 level to be defined as PS1 and PS2, respectively (Figure 5E). Further research
611 should be undertaken to explore the spatiotemporal molecular architecture at
612 single cell resolution and to investigate the mechanism of gut endoderm
613 formation in nonhuman primates.
614

With the spatial transcriptome data of Cynomolgus embryos, we can now glean the primate-specific molecular program by cross-species comparative analysis. We defined species-specific regulons. As expected, most regulons were shared in mice and monkey embryos during germ layer formation, suggesting that the gastrulation event were evolutionally conserved. Interestingly, we found FOXO family showed species-specific usage during gastrulation. FOXO1, FOXO3 and FOXO4 were enriched in macaque, human and mouse respectively (Figure 7G-H), demonstrating that FOXOs may have crucial functions in interspecies evolution. As a key transcription factor to integrate different signals from the insulin/ insulin-like growth factor 1 (IGF-1) signaling pathway, target of rapamycin (TOR) signaling, AMP-activated protein kinase (AMPK) pathway and Jun N-terminal kinase (JNK) pathway (Fontana et al., 2010; Lin et al., 1997; Ma and Gladyshev, 2017; Sun et al., 2017; Tian et al., 2017) to participate in a wide range of important cellular processes such as cell cycle arrest, apoptosis, and metabolism besides its function in stress resistance and longevity (Calissi et al., 2021; Eijkelenboom and Burgering, 2013; Golson and Kaestner, 2016). The preferred cellular mechanisms of FOXO family during early embryo development and beyond is awaiting further investigation.

In summary, our study provides a morphological and molecular atlas for illustrating the dynamics of key processes and regulatory mechanisms during three germ layers formation in primate embryos. Knowledge gained from this work should be valuable for evaluating the interspecies difference and setting a reference for in vitro mimic of monkey embryogenesis. Our work also provide a reasonable working model for human gastrulation. To fully dissect the primate gastrulation, additional studies will be needed to build the single-cell spatiotemporal molecular maps with implementing genetic manipulation and lineage tracing on monkey models.

Figure

Figure 1

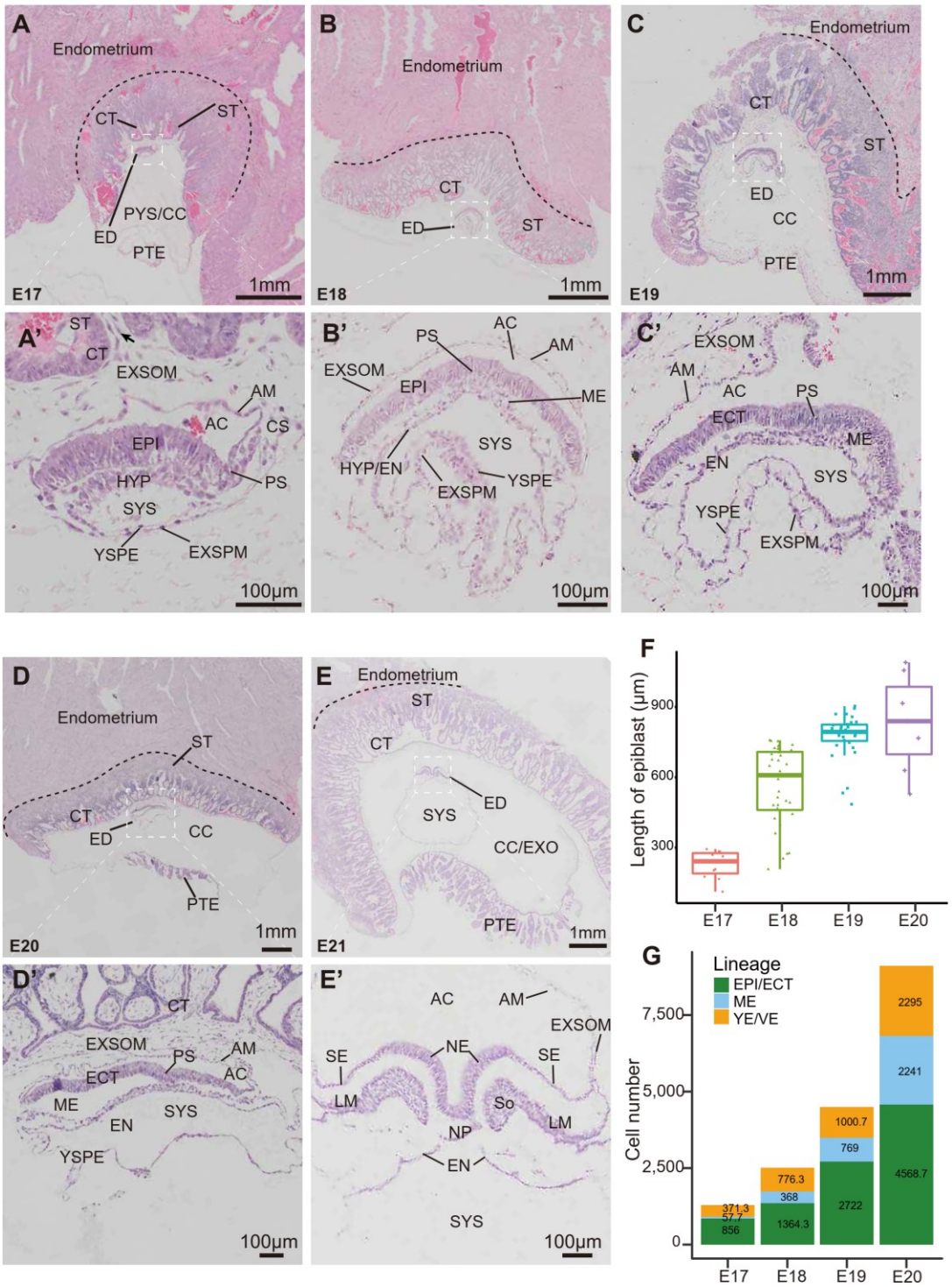

646 **Figure 1 Overview of monkey gastrulation development.**

647 A-E, Haematoxylin and eosin staining of the sections of macaque gastrulating
648 embryos at E17 (A and A'), E18 (B and B'), E19 (C and C'), E20 (D and D') and
649 E21 (E and E'). The image at bottom is a higher magnification of the area boxed
650 on the top. Black arrow points to the extraembryonic mesenchyme has invaded
651 to form the secondary villi. ST, syncytiotrophoblast; CT, cytotrophoblast; PYS,
652 primary yolk sac; CC, chorionic cavity; EXO, exocelom; PTE, parietal
653 trophectoderm; ED, Embryonic disc; EXMC, extra-embryonic mesenchyme cell;
654 AC, amniotic cavity; AM, Amnion; CS, connecting stalk; EPI, epiblast; ECT,
655 ectoderm; PS, primitive streak; ME, mesoderm; HYP, hypoblast; EN, endoderm;
656 YSPE, yolk-sac parietal endoderm; EXSPM, extraembryonic splanchnic
657 mesoderm; EXSOM, extraembryonic somatic mesoderm; SYS, secondary yolk
658 sac.
659 F, The embryo sizes were assessed by the length of sectioned epiblast.
660 G, Bar plot showing total cell numbers in the embryonic germ layers during
661 gastrulation stages. Color represents the germ layer.
662

663 Figure 2

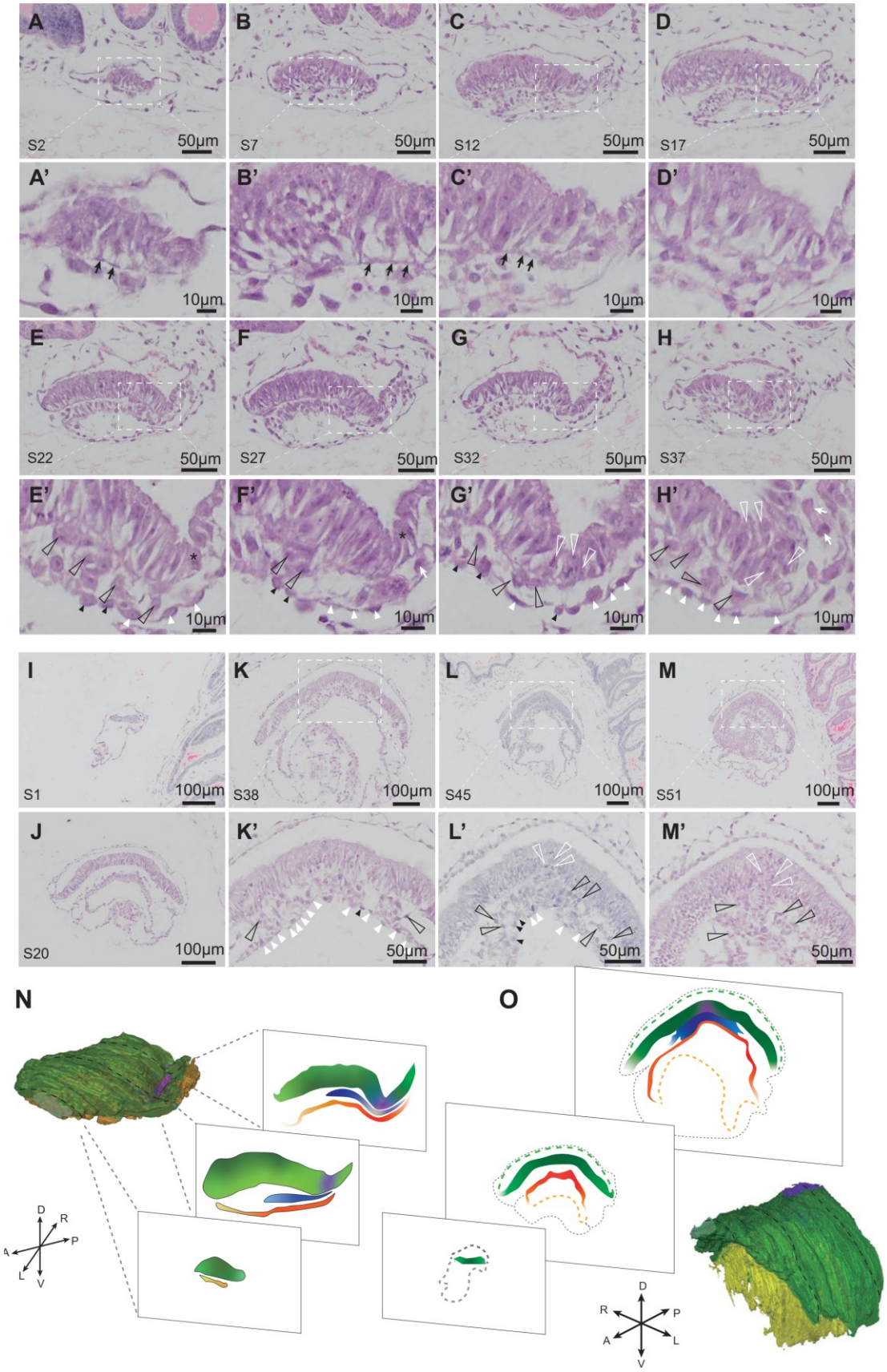

664

665 **Figure 2 Geography of early gastrulation stages in monkey embryos**

666 A-M, Haematoxylin and eosin staining of the sections of macaque gastrulating
667 embryos at E17 (A-H and A'-H') and E18 (I-M and K'-M'). The number of the
668 section is shown in the lower left. High-magnification images are from the boxed
669 region. Black arrows point to basement membrane underlying the epiblast, and
670 white arrows point to extraembryonic mesoderm cells. White open arrowheads
671 indicate gastrulating cells in primitive steak, with black open arrowheads
672 indicating mesoderm cells. White closed arrowheads indicate hypoblast cells,
673 with black closed arrowheads indicating definitive endoderm cells that
674 intercalate in the overlying visceral endoderm epithelium. Asterisks mark
675 embryonic/extraembryonic borders. Scale bar as indicated. A, anterior; P,
676 posterior; L, left; R, right; D, dorsal; V, ventral.
677 N-O, Three-dimensional view of the reconstructed embryo highlighting the
678 primitive streak and germ layers with different colors at E17 (N) and E18 (O).
679 The black dash lines indicate the level of the transversal sections.
680

681 Figure 3

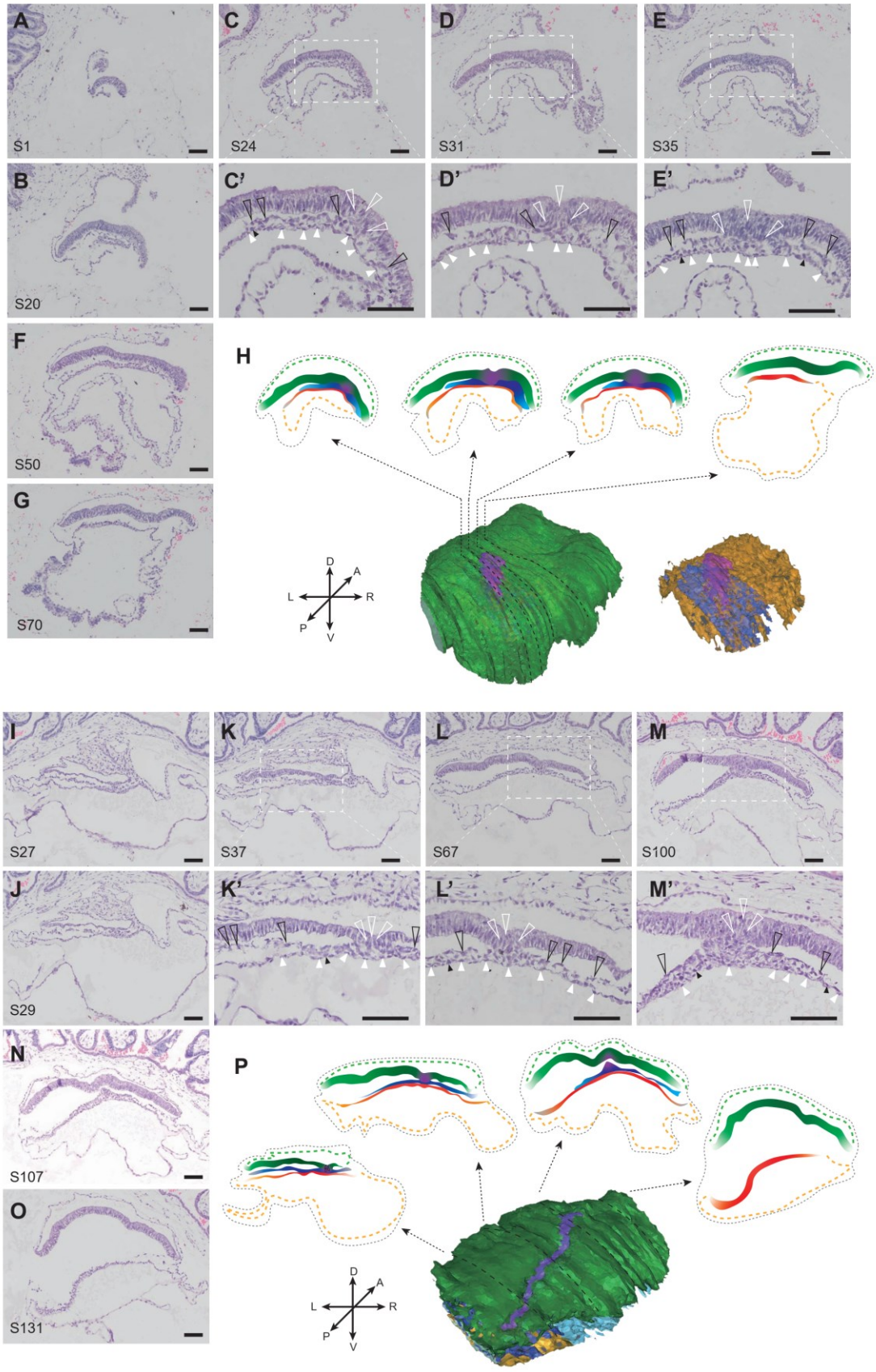

682

683 **Figure 3 Geography of late gastrulation stages in monkey embryos**

684 A-G, Haematoxylin and eosin staining of the sections of macaque gastrulating
685 embryos at E19. The number of the section is shown in the lower left. High-
686 magnification images are indicative of the boxed region. White open
687 arrowheads indicate gastrulating cells in primitive steak, with black open
688 arrowheads indicating mesoderm cells. White closed arrowheads indicate
689 hypoblast cells, with black closed arrowheads indicating definitive endoderm
690 cells that intercalate in the overlying visceral endoderm epithelium. Scale bar,
691 100μm.
692 H, Three-dimensional view of the reconstructed embryo highlighting the
693 primitive streak and germ layers with different colors at E19. The black dash
694 lines indicate the level of the transversal sections.
695 I-O, Haematoxylin and eosin staining of the sections of macaque gastrulating
696 embryos at E20.
697 P, Three-dimensional view of the reconstructed embryo at E20. The black dash
698 lines indicate the level of the transversal sections.
699

700 Figure 4

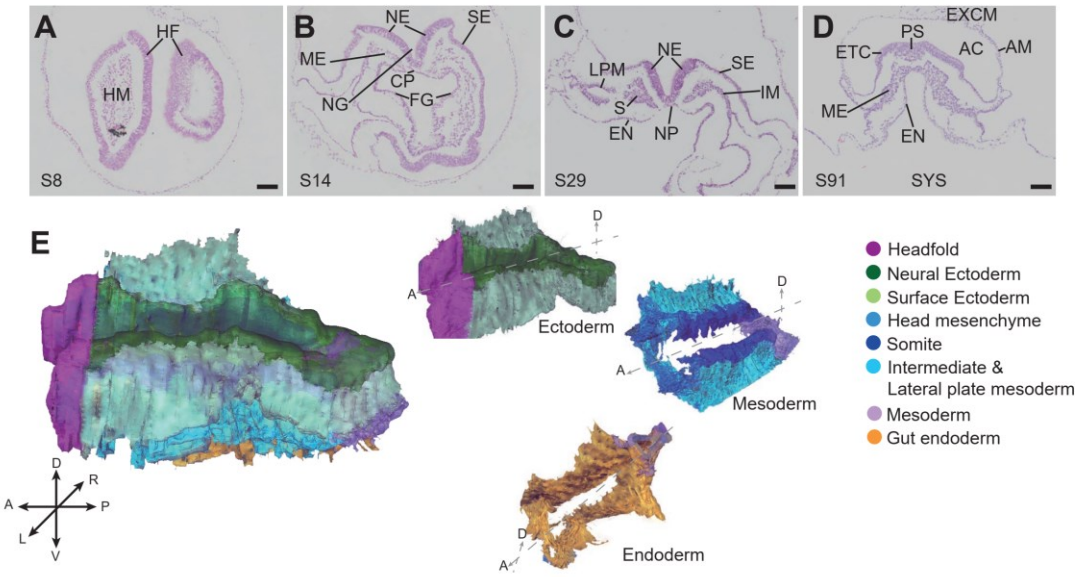

701

702 **Figure 4 Morphology of primate early organogenesis**

703 A-D, Haematoxylin and eosin staining of the sections of macaque
704 organogenesis embryos at E21. The number of the section is signed in the
705 lower left. HF, headfold; HM, head mesenchyme; FG, foregut; NG, neural
706 groove; SE, surface ectoderm; NE, neural ectoderm; CP, chordal plate; ME,
707 mesoderm; S, somite; NP, notochordal plate; IM, intermediate mesoderm; LPM,
708 lateral plate mesoderm; EN, endoderm; PS, primitive streak; ECT, ectoderm;
709 EXMC, extra-embryonic mesenchyme cell; AC, amniotic cavity; AM, Amnion;
710 SYS, secondary yolk sac. Scale bar, 100μm.
711 E, Three-dimensional view of the reconstructed embryo at early organogenesis
712 stage (E21). A, anterior; P, posterior; L, left; R, right; D, dorsal; V, ventral.
713

714 Figure 5

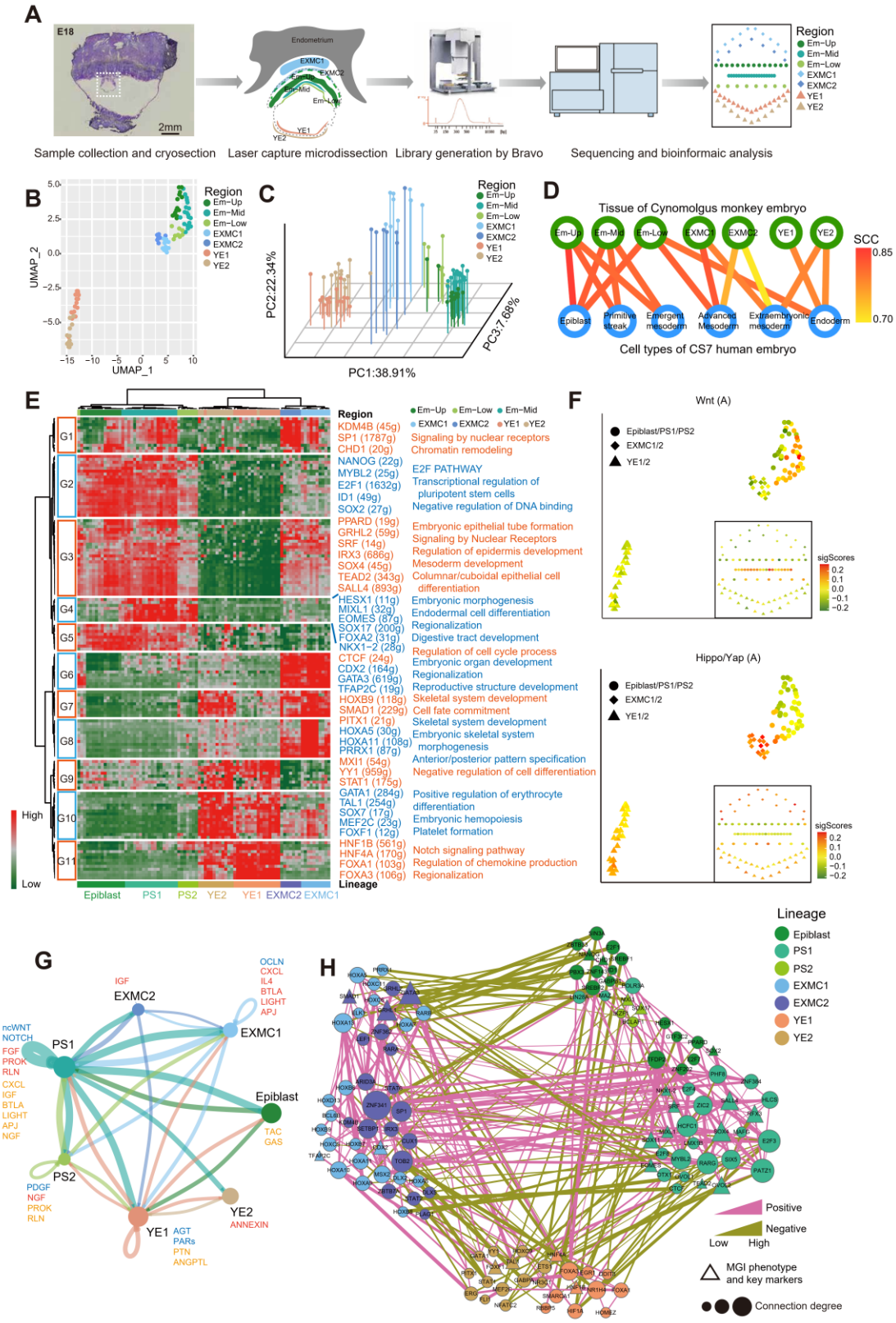

715

716 **Figure 5 Embryonic and extraembryonic spatial molecular dynamic of**
717 **gastrulating monkey embryos**

718 A, Schematic overview of spatial transcriptome of monkey embryo by Geo-seq.
719 The top to bottom of the STGE-plot represents the dorsal-ventral axis of the
720 embryo, which are extra-embryonic mesenchyme tissues (EXMC1/2),
721 embryonic disk (Em-Up, Em-Mid and Em-Low) and yolk-sac endoderm (YE1/2),
722 while left-right does not represent craniocaudal axis of embryo.
723 B, Uniform manifold approximation and projection (UMAP) embedding of
724 monkey samples based on high variable genes (n=5,000) colored by spatial
725 location (n=86).
726 C, 3D-PCA plot based on the regulon activity scores of embryonic and
727 extraembryonic samples showing separate spatial domains.
728 D, The Spearman correlation coefficient of cell population between
729 Cynomolgus monkey spatial (red module) and human single cell annotated cell
730 types (blue module) showing the location of specific cell. The color coding is
731 spearman correlation coefficient (SCC).
732 E, The heatmap of specific regulons (n=192) showing 11 regulon groups in
733 tissue samples of gastrulating monkey embryos with listing of examples of
734 regulon transcription factors (numbers of predicted target genes by SCENIC in
735 the brackets) and the enriched Gene Ontology (GO) terms for each regulon
736 group.
737 F, UMAP and STGE-plot showing the activities of the target genes related to
738 the activated states of the Wnt and Hippo–Yap signalling pathway in primate
739 gastrulation.
740 G, The weighted interaction strength between different tissue types by Cellchat.
741 The autocrine and paracrine (outgoing and incoming) signaling pathways were
742 colored by blue, red and orange respectively. Edge width represents the

communication probability.

H, The co-activation network of tissue specifical regulons based on spearman correlation coefficient (SCC >0.9). The node with different colors represents the highest activity tissue and the edges are the SCC value of two nodes. Violet lines indicate the positive correlation and green lines indicate negative correlation. A wider edge signifies higher correlation. Triangle nodes denote transcription factors with mouse knockout gastrulation phenotype in MGI database. The larger the node, the more connections to other regulons.

751 Figure 6

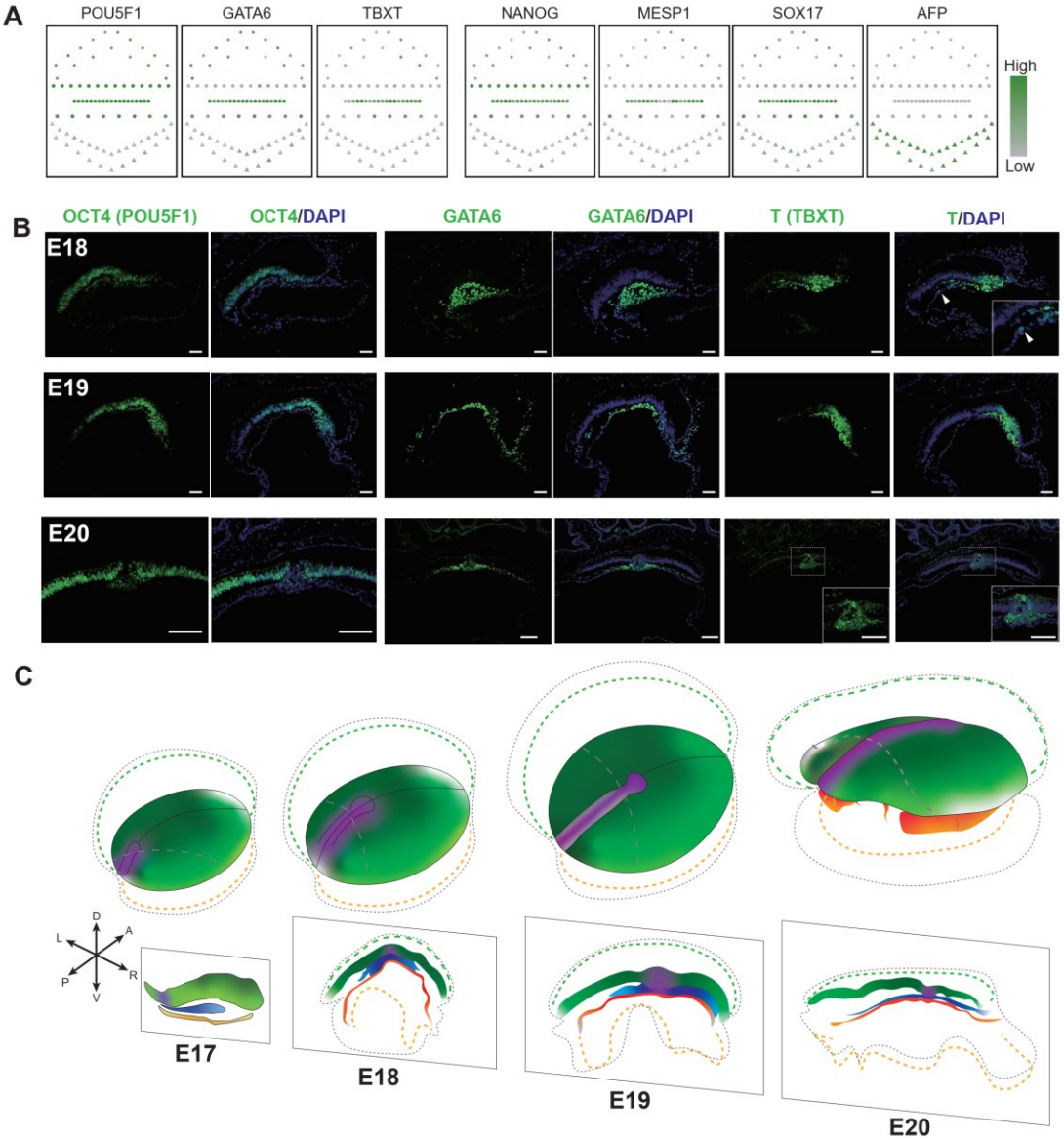

752

753

754 **Figure 6 Spatiotemproal cellular and molecular characteristics**

755 A, STGE-plot showing the relative expression of marker genes related to the
756 germ layers and primitive streak in primate gastrulation. Color code represents
757 the relative expressed levels.
758 B, Representative immunofluorescent images of embryos at E18, E19 and E20
759 for OCT4 (green), GATA6 (green), TBXT (green) and DAPI (blue). White closed
760 arrowheads indicate gastrulating cells that intercalate in the hypoblast. High-
761 magnification images are indicative of the boxed region. Scale bar, 100μm.
762 C, Scheme of monkey gastrulation development. A, anterior; P, posterior; L, left;
763 R, right; D, dorsal; V, ventral. The grey dash lines on epiblast indicate the level
764 of the transversal sections.

765 Figure 7

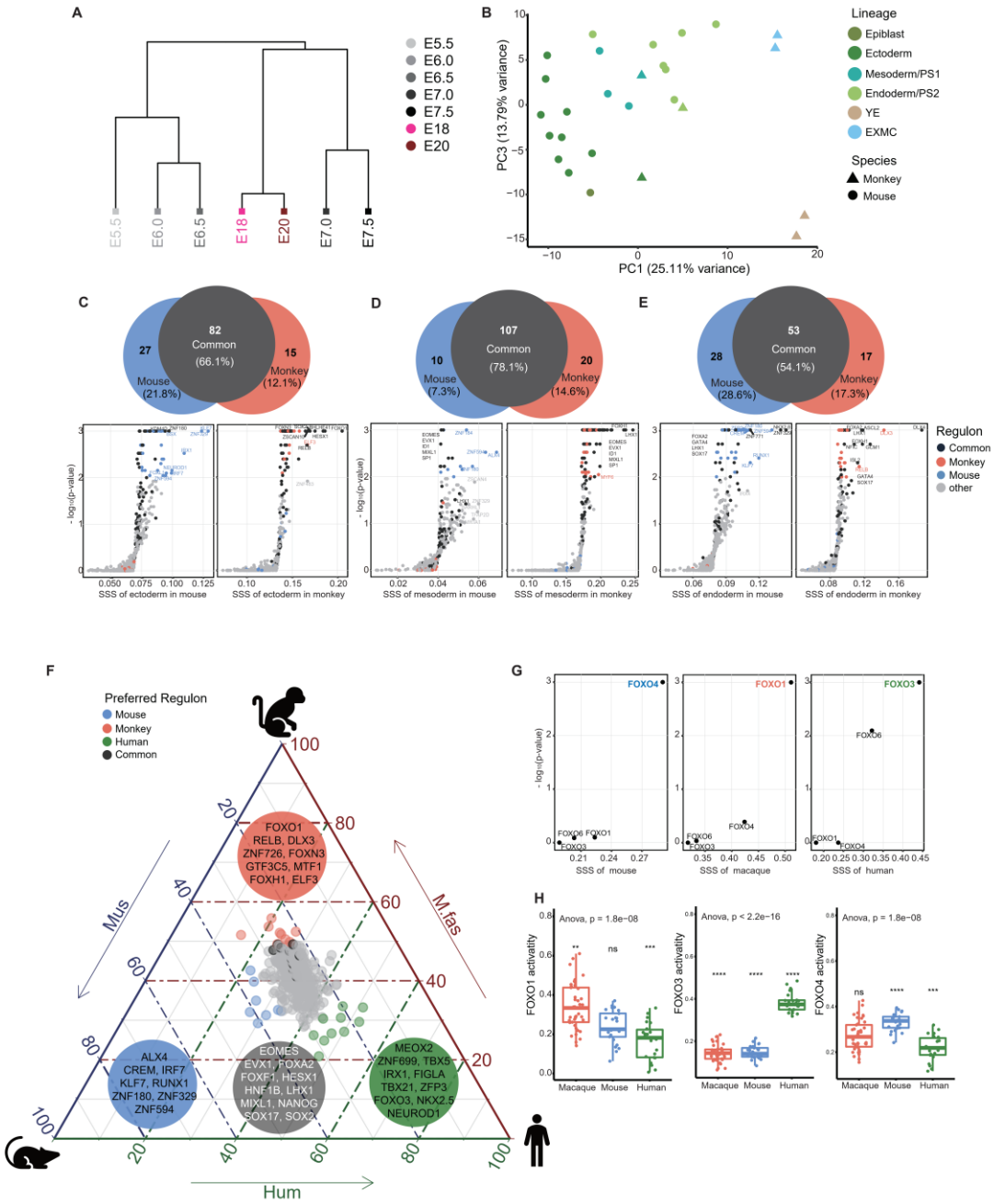

766

767 **Figure 7 Cross-species spatial transcriptomic analysis reveals**
768 **gastrulation developmental differences among mice, monkeys and**
769 **humans**

770 A, Hierarchical clustering analysis of mouse and monkey whole embryos in
771 different gastrulation stages based on averaged dynamic regulons (n=451).
772 B, PCA analysis showing the lineage difference between mouse and monkey.
773 YE, yolk-sac endoderm; EXMC, extra-embryonic mesenchyme tissues.
774 C-E, Species specific regulons between mouse and monkey in ectoderm,
775 mesoderm and endoderm embryogenesis, respectively. Venn plot showed the
776 lineage species specific and common regulons. The scatter plot showed the
777 significant and specific regulons in different species germ layer. SSS,
778 species/spatial domain-specificity score. Color code the specific type of
779 regulons.
780 F, Ternary plot of the most divergent species-specific regulons in gastrulation
781 between mouse, monkey and human. Top 10 regulons were colored and listed
782 based on species - specificity score (SSS).
783 G. Species-specificity score of FOXO regulons between mouse, monkey and
784 human gastrulation embryonic tissue.
785 H, The activities of FOXO regulons between mouse, monkey and human
786 gastrulation embryonic tissue.

787

788

SUPPLEMENTAL INFORMATION

Supplemental Information includes Supplemental Experimental Procedures, eight figures, and three tables and can be found with this article online at ..

ACKNOWLEDGMENTS

We thank W. Ji for critical discussions, S.Suo for help of data analysis, and J. Xu, J.Zhang, M.Wang, L.Qin for experimental support. This work was supported in part by National Key R&D Program of China (2018YFA0801402, 2018YFA0107200, 2019YFA0801400), the "Strategic Priority Research Program" of the Chinese Academy of Sciences (XDA16020404 and XDA16010308), National Natural Science Foundation of China (31871456, 32100483), Guangdong Basic and Applied Basic Research Foundation (2019B151502054, 2019A1515110985).

AUTHOR CONTRIBUTIONS

N.J. and G.P. conceived the study. G.P., N.J. and W.S. supervised the project. G.P., N.J., W.S. and G.C. designed the experiments. G.C. and S.F. conducted the histology and IF and analyzed the data, G.C. and L.W. contributed to the 3D reconstruction of the histological sections, W.S., Y.Y., X.H., X.L., Y.D. and P.Z. performed samples collection, G.C. and G.P. performed the Geo-seq experiments and analyzed the spatial transcriptome data, K.T. and J.C. performed tissue staining, G.C., G.P., P.P.L.T. and N.J. wrote the paper with the help of all other authors.

DECLARATION OF INTERESTS

The authors declare no competing interests.

816 # STAR Methods

817 ## KEY RESOURCES TABLE

REAGENT or RESOURCE	SOURCE	IDENTIFIER
Antibodies		
OCT4	Santa Cruz Biotechnologies	Cat#sc-5279
GATA6	Cell Signaling Technology	Cat#5851
Brachyury /T	R&D Systems	Cat#AF2085
DAPI	Sigma-Aldrich	Cat#28718-90-3
Biotin-SP (long spacer) AffiniPure Donkey Anti-Goat IgG (H+L)	Jackson Immuno	Cat#705-065-147; RRID: AB_2340397
Biotin-SP (long spacer) AffiniPure Donkey Anti-Rabbit IgG (H+L)	Jackson Immuno	Cat#711-065-152; RRID: AB_2340593
Biotin-SP (long spacer) AffiniPure Donkey Anti-Mouse IgG (H+L)	Jackson Immuno	Cat#715-065-150; RRID: AB_2307438
Normal Donkey Serum	Jackson Immuno	Cat#017-000-121; RRID: AB_2337258
Chemicals, peptides, and recombinant proteins		
Tissue freezing medium (OCT)	Leica Microsystems	Cat#020108926
Cresyl violet acetate	Sigma-Aldrich	Cat#C5042
dNTP mix	Takara	Cat#4030
RiboLock RNase Inhibitor	Roche	Cat#Eo0382
SuperScript II reverse transcriptase	Invitrogen	Cat#18064-014
KAPA HiFi HotStart ReadyMix	KAPA Biosystems	Cat#KK2601
VAHTS DNA Clean Beads	Vazyme	Cat#N411-02
Betaine solution	Sigma-Aldrich	Cat#B0300-1VL
Guanidine isothiocyanate solution	Invitrogen	Cat#15577-018
Antigen retrieval solution	Dako	Cat#S169984
Fluoromount-G	SouthernBiotech	Cat#G1417-T937
Critical commercial assays		
Qubit dsDNA HS Assay Kit	Invitrogen	Cat#Q32854
TruePrep DNA library pre kit V2	Vazyme	Cat#TD502-02
Alexa Fluor™ 488 Tyramide SuperBoost™ Kit, streptavidin	Thermofisher	Cat#B40932
Deposited data		

Raw and processed Geo-seq data of gastrulating macaque	This paper	GEO: GSE182838
The single cell RNA-seq data of monkey gastrulating embryo (E13, E14, E16 and E17)	(Nakamura et al., 2016)	GEO: GSE74767
The spatiotemporal transcriptome of gastrulating mouse embryos	(Peng et al., 2019)	GEO: GSE120963
RNA-seq data of spatial sectioned human gastruloids	(Moris et al., 2020)	GEO: GSE123187
Single-cell transcriptome of human CS7 gastrula	(Tyser et al., 2021)	ArrayExpress: E-MTAB-9388
Experimental models: Organisms/strains		
Cynomolgus monkeys	Institute of Zoology and Kunming Institute of Zoology, Chinese Academy of Sciences (CAS)	N/A
Oligonucleotides		
3'CDS primer: AAGCAGTGGTATCAACGCAGAGTACTTTTTTTTTTTTTTTTTTTTTTTTTTTTTTVN	(Chen et al., 2017)	N/A
TSO primer: AAGCAGTGGTATCAACGCAGAGTACAT/rG//rG//iXNA_G/	(Chen et al., 2017)	N/A
IS PCR primer: AAGCAGTGGTATCAACGCAGAGT	(Chen et al., 2017)	N/A
mfGAPDH-qPCR-F: AACAGGGTGGTGGACCTCAT	(Nakamura et al., 2016)	N/A
mfGAPDH-qPCR-R: TTCCTCTTGTGCTCTCGCTG	(Nakamura et al., 2016)	N/A
mfGATA4-qPCR-F: TGGCTATAGCAGAGAATACCTTTGAACCA	(Nakamura et al., 2016)	N/A
mfGATA4-qPCR-R: ACAGGTTTGTGGGTTAGGGAGGGT	(Nakamura et al., 2016)	N/A
mfPOU5F1-qPCR-F: GGGAGGAGCTAGGGAAAGAGAACCTA	(Nakamura et al., 2016)	N/A

mfPOU5F1-qPCR-R: CCCCCACCCGTTGTGTTCCCA	(Nakamura et al., 2016)	N/A
Software and algorithms		
HISAT2	(Pertea et al., 2016)	http://daehwankimlab.github.io/hisat2/
R Studio	Rstudio	https://rstudio.com/products/rstudio/ download/
R	The R Foundation	https://cran.r-project.org/mirrors.html
Seurat	(Stuart et al., 2019)	https://satijalab.org/seurat/
SPOTlight	(Elosua-Bayes et al., 2021)	https://github.com/MarcElosua/SPOTlight
Vision	(DeTomaso et al., 2019)	www.github.com/YosefLab/VISION
Ucell	(Andreatta and Carmona, 2021)	https://github.com/carmonalab/UCell
SCENIC	(Aibar et al., 2017)	http://scenic.aertslab.org
WGCNA	(Langfelder and Horvath, 2008)	https://horvath.genetics.ucla.edu/html/CoexpressionNetwork/Rpackages/WGCNA/
Cellchat	(Jin et al., 2021)	https://github.com/sqjin/CellChat
Cytoscape (v.3.8.2)	(Otasek et al., 2019)	https://cytoscape.org/
Metascape	(Zhou et al., 2019)	http://metascape.org
clusterProfiler (version 3.12.0)	(Yu et al., 2012)	https://bioconductor.org/packages/release/bioc/html/clusterProfiler.html
TCseq	(Mengjun, 2019)	https://bioconductor.org/packages/release/bioc/html/TCseq.html
FIJI	(Schindelin et al., 2012)	https://imagej.net/Fiji
Vaa3D (version 3.5)	(Peng et al., 2010)	https://github.com/Vaa3D/release/releases/
Amira	Thermofisher	https://www.thermofisher.cn/cn/zh/home/electron-microscopy/products/software-em-3d-vis/amira-software.html
Other		
VS120	Olympus	N/A

BX51	Olympus	N/A

RESOURCE AVAILABILITY

Lead contact

Further information and requests for resources and reagents should be directed to and will be fulfilled by the Lead Contact, Guangdun Peng (peng_guangdun@gibh.ac.cn).

Materials availability

Unique materials generated in this study are available from the Lead Contact without restriction.

Data and code availability

The Cynomolgus monkey spatiotemporal RNA-seq raw and processed data have been deposited in the Gene Expression Omnibus database under accession number GSE182838, and also can be downloaded from our website. Custom code and scripts are available from methods details and github. All other data supporting the findings of this study are available from the corresponding author upon request.

EXPERIMENTAL MODEL AND SUBJECT DETAILS

All monkey experiment procedures were under the guidance of the Ethics Committee of the Institute of Zoology and Kunming Institute of Zoology, Chinese Academy of Sciences (CAS). The gastrulating embryos of Cynomolgus monkeys (*Macaca fascicularis*) from natural conception and in

840 vitro fertilization (IVF) were both used in this study. The procedures in
841 Cynomolgus monkeys for oocyte collection, intra-cytoplasmic sperm injection,
842 pre-implantation embryo culture, and transfer of pre-implantation embryos into
843 foster mothers were performed as described previously (Niu et al., 2019;
844 Yamasaki et al., 2011). The day when the intra-cytoplasmic sperm injection was
845 performed was designated as embryonic day (E) 0. For the detection of
846 pregnancy of early post-implantation embryos, implanted embryos were
847 monitored by ultrasound scanning around E14 and the implanted uterus was
848 surgically removed and bisected for the isolation of embryos.
849 For naturally mated embryos, health adult female and male monkeys aged from
850 7-8 years were individually kept in an animal room with humidity at 40-70% and
851 temperature at 18-26 °C and exposed to a 12:12 light–dark cycle. The female
852 monkeys were observed at least two normal menstrual cycles confirmed by
853 virginal bleed before being allowed to mating with male monkeys. The first day
854 of bleeding was defined as day 1 of menses once menstrual cycle start. Then
855 venous blood was collected at 09:00 AM on menses days 7 to 18, and a male
856 monkey was allowed to mating with the female monkey. Blood serum was
857 separated by centrifugation and concentrations of E2 and P4 were assayed
858 using a chemiluminescent immunoassay. Once the peak of E2 was detected,
859 then the next day was defined as the day of ovulation and fertilization, and the
860 concentration of blood E2 and P4 were continuously measured. The pregnancy
861 was confirmed by the low level of E2, increased level of P4 and ultrasonography.
862

863 # METHOD DETAILS

864 **Monkey embryo H&E staining and immunofluorescent analysis**

865 Monkey post-implantation embryos by IVF procedure were harvested at

866 different stage from embryonic day 17(E17) to E21 every day (at least two
867 embryos in each stage), and whole embryos were fixed in 4%
868 paraformaldehyde (PFA) at 4°C overnight. The procedures of paraffin
869 embedding were carried out, and the embedding embryos were transversely
870 sectioned at a thickness of 5 μm. The sections were stained by H&E staining
871 and immunofluorescent staining as previously reported (Feng et al., 2017). In
872 brief, after dewaxed and rehydrated, the slides were stained in hematoxylin
873 solution for 30 sec and counterstained in eosin solution for 10 sec. For
874 immunofluorescence staining, the sections were incubated with primary
875 antibody in hybridization buffer overnight at 4 °C after blocked, and incubated
876 with secondary antibody for 1 hour (h) at room temperature. The sections were
877 counterstained with 4′,6′-diamidino-2-phenylindole (DAPI) and mounted with
878 mounting medium. Bright field images and fluorescent images were collected
879 on an Olympus VS120 and Olympus BX51 microscope respectively, and
880 aligned manually using Adobe Photoshop CC.

881 **Determination of gastrulation cell number and mitotic activity**

882 The number of cells contained in epiblast/ectoderm, mesoderm and
883 hypoblast/endoderm were determined by counting nuclei on every section of
884 the gastrulating embryos. The total score was then adjusted by applying
885 Abercrombie's correction formula (Abercrombie, 1946) to give an estimate of
886 the actual cell number. In detail, the average number of cells per section (*P*):

887 $$P = A\frac{M}{L+M}$$

888 *A* is the crude count of number of nuclei fragments, *M* is the thickness of the
889 section (*M*=5μm in this study), and L the average length of the nuclei (*L*=10μm
890 in this work).

891 Cell cycle times can be calculated from the equation (Snow, 1977), C_t means
892 the cell number at *t* stage:

893 $$T = \frac{\Delta t}{C_{t+1}/C_t}$$

894

895 **3D reconstructions of gastrulating monkey embryos**

896 The Vaa3D (version 3.5) and Amira (version 6.0.1) were used for the 3D
897 reconstruction process, consisting of alignment, segmentation and visualization
898 (de Bakker et al., 2016; Peng et al., 2010). In brief, grey scale processing was
899 performed by Photoshop CC (Adobe Systems), and alignment of the stitched
900 serial images was mainly implemented by manual after automatically
901 adjustments. The aligned 3D images were segmented into epiblast/ectoderm,
902 primitive streak, hypoblast/endoderm and mesoderm. Then, triangulated
903 surface files were made using the *SurfaceGen* function, and triangle reduction
904 (*Simplify*) and surface smoothing (*SmoothSurface*) were also applied for
905 visualization. Besides, the Vaa3D was also applied to aligned sections to
906 visualize the 3D structure of specific tissues.

907 **Spatial molecular profiling of monkey embryos**

908 The spatial transcriptome of gastrulating embryos was obtained according to
909 Geo-seq protocol with minor modifications (Peng et al., 2019). Briefly, whole
910 embryos (two monkey embryos at E18 and one at E20 from natural conception)
911 were embedded in OCT (Leica Microsystems, catalogue no. 020108926), and
912 cryo-sectioned in the coronal plane serially from the anterior region to the
913 posterior region at a thickness of 20 μm. Sections were transferred onto LCM
914 PEN membrane slides, fixed immediately by ethanol and stained with 1% cresyl
915 violet acetate in 75% ethanol solution (Sigma-Aldrich). The embryonic tissue
916 was divided into upper, middle and lower layer, and the extraembryonic tissue
917 was divided into extra-embryonic mesenchyme 1/2 and yolk-sac endoderm 1/2

918 based on the good morphology sections. Populations of 5-50 cells were
919 collected by laser microdissection, and total RNA pellets were dissolved in lysis
920 solution, followed by reverse transcription using SuperScript II reverse
921 transcriptase (Invitrogen), whole transcription amplification with KAPA HiFi
922 HotStart ReadyMix (2X; KAPA Biosystems). The PCR product of LCM samples
923 were used for automated single-cell RNA-Seq library construction based on the
924 Bravo robot station(Cui et al., 2019). In brief, PCR product were purified using
925 0.75X AMPure XP beads (Agencourt), quantified with Qubit dsDNA HS Assay
926 Kit (Thermo Fisher) on Envision (PerkinElmer), and cDNA library was
927 constructed by DNA Library Prep Kit V2 for Illumina (Vazyme) and sequenced
928 on an Illumina Nova 6000 instrument using a 150 bp paired-end-reads setting.

929 QUANTIFICATION AND STATISTICAL ANALYSIS

930 Processing of RNA-seq data

931 Sequencing quality of raw sequencing data was evaluated by fastp (Chen et al.,
932 2018). The genome sequence Macaca_fascicularis_5.0 for Cynomolgus
933 monkeys (*Macaca fascicularis*) were obtained from the Ensemble
934 (https://asia.ensembl.org/index.html). Reads were mapped to the
935 Macaca_fascicularis_5.0 genome assemblies by HISAT2 (Pertea et al., 2016)
936 using default settings. Mapping ratio was calculated based on the number of
937 mapped reads and total reads for each sample. All mapped reads were
938 processed by StringTie(Pertea et al., 2016) to quantify gene expression levels
939 (measured by TPM and FPKM, Transcripts Per Kilobase per Million mapped
940 reads and Fragment Per Kilobase per Million mapped reads respectively) using
941 default parameters. Seurat package (version 3.1.5) (Stuart et al., 2019) was
942 applied to dimensionality reduction analysis in R (version 4.0.3). Gene
943 expressed in at least two samples across all samples were selected for further

944 analysis. After filtering, data in each sample were normalized, the 5,000 most
945 variable genes were identified with *vst* method, and the expression levels of
946 these genes were scaled before performing Principal Component Analysis
947 (PCA) in variable gene space. Next, 5 principal components were used for
948 graph-based clustering (resolution = 2) and UMAP dimensionality reduction
949 was computed using *RunUMAP* function with default parameters. The
950 Spearman correlation coefficient (SCC) of spatial domain between embryonic
951 replicates or developmental stages were calculated based on average
952 expression of all gene.
953

954 **Identification of differentially expressed genes (DEGs) and clustering**
955 **analysis**

956 Gene expression levels for each sample were $\log_2$ (TPM+1) transformed and
957 then combined 5,000 most variable genes with top 150 highest and lowest
958 Principal Component (PC) loading genes (by using *FactorMineR* in R) from
959 PC1-5 to identify the DEGs. In total, 1,305 genes were identified as DEGs.
960 Finally, unsupervised hierarchical clustering was performed using the *hclust*
961 function Ward's method (ward.D2) to determine the final spatial domains of
962 embryonic and extraembryonic tissues based on the expression profile of DEGs.
963

964 **Integrating scRNA-seq and spatial transcriptome**

965 To investigate the architecture of the cell-type distribution in spatial
966 transcriptome, we integrate both single-cell and spatial transcriptomics data of
967 monkey gastrulating embryo *in vivo* to infer the spatial locations of different cell
968 types in a tissue. The single cell RNA-seq data of monkey gastrulating embryo
969 (E13, E14, E16 and E17) from GSE74767(Nakamura et al., 2016), and apply

970 *FindAllMarkers* function of Seurat pipeline to identify cluster markers.
971 SPOTlight, a deconvolution algorithm that built upon a non-negative matrix
972 factorization (NMF) regression algorithm was used for cell-type deconvolution
973 in spatial transcriptome (Elosua-Bayes et al., 2021). In brief, SPOTlight
974 factorizes the normalized scRNA-seq gene expression matrix into two lower
975 dimensionality matrices using NMF, and cell-level topic distribution matrix is
976 used to learn the cell-type specific topic profiles through a Non-Negative Least
977 Squares regression (NNLS). The weights of each cell-type specific topic profile
978 represent the cell-type proportions across all samples in spatial transcriptome.
979 Furthermore, we used the averages of single-cell detectable gene expression
980 in the same annotated cell type and spatial samples at the same location to
981 calculate the SCC.
982

983 **Pathway activity analysis and epithelial-mesenchymal transition scores**
984 **analysis**

985 To identify the key biological properties of spatial samples, Vision (DeTomaso
986 et al., 2019; Zhang et al., 2020) and Ucell (Andreatta and Carmona, 2021) were
987 applied to perform functional enrichment analyses. The homologous target
988 genes of WNT, BMP, FGF, NODAL and Hippo/Yap signaling pathways between
989 monkey and mouse gastrulating (Peng et al., 2019) were used as signatures of
990 *vision* analysis. In addition, we input the gene signatures of MSigDB, which
991 curated by the Broad institute, to explore the transcriptional effects of regions.
992 To evaluate the epithelial–mesenchymal transition (EMT) of epiblast cells,
993 scoring EMT based on the Mann-Whitney U statistic (Andreatta and Carmona,
994 2021). The EMT-inducing transcriptions factors (EMT-TFs) zinc-finger E-box-
995 binding family (ZEB1 and ZEB2), basic helix–loop–helix transcription factors
996 (TWIST1 and TWIST2) and snail family transcriptional repressor (SNAI1 and

997 SNAI2) were included as signature of mesenchymal state. The markers
998 associated with the mesenchymal state vimentin (VIM), fibronectin and β1 (FN1)
999 and matrix metalloproteinase (MMP2) and the markers related to the epithelial
1000 state E-cadherin (CDH1), grainyhead like transcription factor (GRHL2),
1001 epithelial cell adhesion molecule (EPCAM), Occludins (OCLN), Claudins
1002 (CLDN4 and CLDN7) and cytokeratins (KRT19) were also add into Ucell
1003 analysis (Chakraborty et al., 2020; Dongre and Weinberg, 2019; Lamouille et
1004 al., 2014). The EMT score is the difference of epithelial score minus
1005 mesenchymal score (E-M), and the higher EMT scores, the more epidermal-
1006 like state.

1007 **Reconstruction of regulons in embryonic and extraembryonic tissues**

1008 For inferring Cynomolgus monkey's gene regulatory network (GRN) using
1009 SCENIC (Aibar et al., 2017), common genes listed in the Cynomolgus
1010 monkeys–humans one-to-one annotation table were used(Nakamura et al.,
1011 2016). 17,019 common genes were first filtered to exclude all genes detected
1012 in fewer than two samples, and then were used to identified TF-gene co-
1013 expression modules. Subsequently, those modules are refined via RcisTarget
1014 by keeping only those genes than contain the respective transcription factor
1015 binding motif. Finally, SCENIC found 323 regulons in monkey gastrulating
1016 embryos, whose regulatory activities were represented by AUCell values. To
1017 identify regulons associated with spatial domains of gastrulating monkey
1018 embryos, we used the regulon activity score for each sample to perform PCA,
1019 heatmap display and network analysis (Peng et al., 2016; Peng et al., 2019).
1020 Regulons shared in 250 most variable regulons and top 100 highest and lowest
1021 PC loading regulons from PC1-3 were defined as specific regulons. For network
1022 visualization, the regulon was assigned to the tissue with highest average
1023 regulon activity score. The SCC was calculated in the same lineage, and the

1024 absolute value was greater than 0.95 for further analysis. The edge weights
1025 were proportional to the SCC values of two correlated nodes.

1026 **Co-expression gene network and interaction analysis**

1027 To identify biologically relevant patterns of spatial samples, we performed
1028 weighted gene co-expression network analysis using R package WGCNA
1029 (Langfelder and Horvath, 2008). Briefly, a soft power threshold of 10 was set to
1030 constructed unsigned network and the minimum module size was set to 10
1031 genes. Eight gene modules with significant correlation in the seven spatial cell
1032 populations were used to draw gene modules for each cell type. Only top 30
1033 genes with highest 100 correlation coefficient values in each module were kept
1034 when visualizing the modules with Cytoscape (v.3.8.2)(Otasek et al., 2019).
1035 To quantitatively infer and analyze intercellular communication networks,
1036 Cellchat was applied to predict potential interaction probability scores (Jin et al.,
1037 2021). Human gene names were converted to Cynomolgus monkey genes
1038 using orthology data from monkeys–humans one-to-one annotation table, with
1039 17,542 genes in common between the two species (Nakamura et al., 2016).
1040 We use the tissue type of spatial sample based on regulon activity clustering
1041 as label information, and calculated an aggregated interaction probability by
1042 Cellchat based on the expression level of ligand–receptor pairs.

1043 **Functional enrichment analysis and phenotype analysis**

1044 We applied Metascape (Zhou et al., 2019) (http://metascape.org), KOBAS-i
1045 (KOBAS intelligent version, version 3.0) (Bu et al., 2021) and R package
1046 clusterProfiler (version 3.12.0) (Yu et al., 2012) to perform Gene Ontology and
1047 pathways enrichment analysis for each group of DEGs and regulon TFs. The
1048 TFs which display strong gastrulation phenotypes from Mouse Genome
1049 Information (MGI) database were highlighted and visualized in the regulon

1050 network.

1051

1052 **Cross-species comparative analysis**

1053 The spatiotemporal transcriptome of gastrulating mouse embryos was
1054 generated in our previous work (Peng et al., 2019) (GSE120963), and used the
1055 RNA-seq data of spatial sectioned human gastruloids (Moris et al., 2020)
1056 (GSE123187) and single cell transcriptome (E-MTAB-9388) to assess human
1057 gastrulating embryos. For comparison of the gene expression among mouse,
1058 Cynomolgus monkeys and human, ortholog genes of these three species from
1059 Ensemble were used for further analysis (Nakamura et al., 2016). To reveal the
1060 temporal pattern of time course sequencing data, the TCseq package (Mengjun,
1061 2019) was performed to classify the dynamic regulons into various types of
1062 clusters, with the genes in each cluster were then processed for functional
1063 enrichment analysis. Then the total of 451 different regulons across five stages
1064 of gastrulation were used for hierarchical clustering and PCA analysis.
1065 To quantify the species germ layer specificity of a regulon, an entropy-based
1066 strategy was modified from regulon specificity score (RSS) (Peng et al., 2019;
1067 Suo et al., 2018). All 490 regulon gene lists which calculated by SCENIC in
1068 monkey gastrulating embryos were reanalyzed in natural logarithms
1069 transformed expressed matrix of three species by AUCell package (version
1070 1.16.0). Then the Jensen–Shannon divergence (JSD) algorithm was used to
1071 identify species-spatial domain-specific regulons by philentropy package
1072 (version 0.5.0) (Drost, 2018). Finally, for distribution of each regulon P_1 and
1073 predefined pattern P_2, the species/spatial domain- specificity score (*SSS*)
1074 between P_1 and P_2 was defined by converting JSD to a similarity score:

1075 $$SSS = 1 - \sqrt{JSD(P_1, P_2)}$$

1076 To evaluate the significance of regulon specificity in each species spatial

domain, the regulon-activity score was permuted across all samples 1,000 times, then calculated *SSS*, and finally a permutation *p* value was calculated as the number of times that $SSS_{permutation} > SSS_{true}$ divided by 1,000. Only the significant regulons ($P < 0.01$), which were specifically activated in species-spatial domains, were kept for downstream analysis. Ternary plot was applied to show the proportion of *SSS* mice, monkeys and humans.

SUPPLEMENTAL INFORMATION

Figure S1

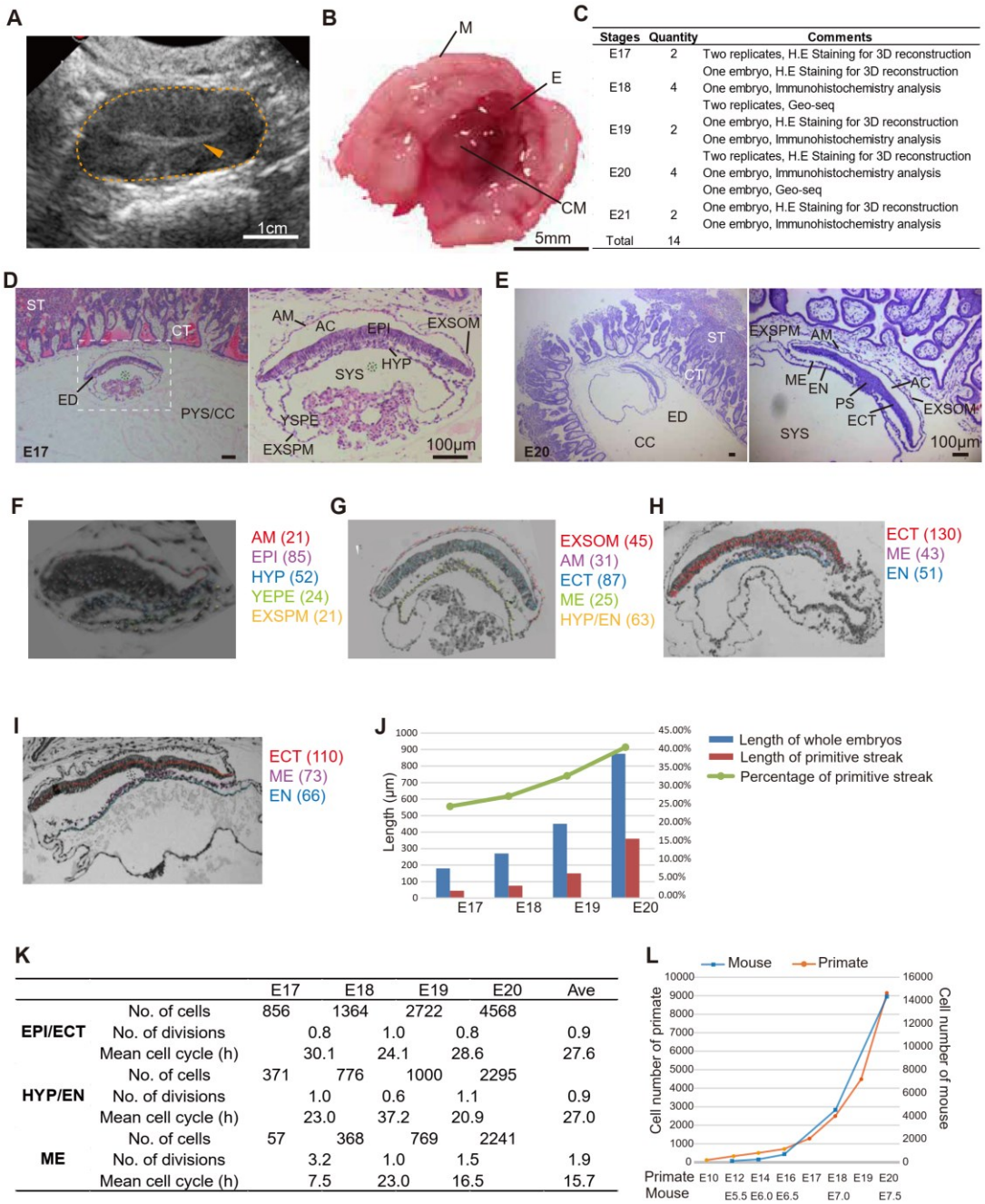

Stages	Quantity	Comments
E17	2	Two replicates, H.E Staining for 3D reconstruction
E18	4	One embryo, H.E Staining for 3D reconstruction One embryo, Immunohistochemistry analysis Two replicates, Geo-seq
E19	2	One embryo, H.E Staining for 3D reconstruction One embryo, Immunohistochemistry analysis
E20	4	Two replicates, H.E Staining for 3D reconstruction One embryo, Immunohistochemistry analysis One embryo, Geo-seq
E21	2	One embryo, H.E Staining for 3D reconstruction One embryo, Immunohistochemistry analysis
Total	14	

K

		E17	E18	E19	E20	Ave
EPI/ECT	No. of cells	856	1364	2722	4568	
	No. of divisions	0.8	1.0	0.8		0.9
	Mean cell cycle (h)	30.1	24.1	28.6		27.6
HYP/EN	No. of cells	371	776	1000	2295	
	No. of divisions	1.0	0.6	1.1		0.9
	Mean cell cycle (h)	23.0	37.2	20.9		27.0
ME	No. of cells	57	368	769	2241	
	No. of divisions	3.2	1.0	1.5		1.9
	Mean cell cycle (h)	7.5	23.0	16.5		15.7

1089 **Figure S1 Macaque gastrulating embryos.**

1090 A, Ultrasound diagnosis of the monkey's recipient uterus for the implantation of
1091 transplanted embryos at E17. Dashed circles indicate the uterus and
1092 arrowheads indicate the chorionic cavity. Scale bars, 1 centimeter.
1093 B, Images of dissected monkey uterus at gastrulation stage. M, myometrium;
1094 E, endometrium; CM, chorionic membranes. Scale bars, 5 millimeters.
1095 C, Summary of collected embryos during gastrulation.
1096 D, Haematoxylin and eosin staining of the section of replicate embryo at E17.
1097 The image at right is a higher magnification of the area boxed on the left. ST,
1098 syncytiotrophoblast; CT, cytotrophoblast; PYS, primary yolk sac; CC, chorionic
1099 cavity; ED, Embryonic disc; AC, amniotic cavity; AM, Amnion; EPI, epiblast;
1100 HYP, hypoblast; YSPE, yolk-sac parietal endoderm; EXSPM, extraembryonic
1101 splanchnic mesoderm; EXSOM, extraembryonic somatic mesoderm; SYS,
1102 secondary yolk sac. Scale bar, 100μm
1103 E, Haematoxylin and eosin staining of the section of replicate embryo at E20.
1104 The left is the lower magnification images. Scale bar, 100μm
1105 F-I, The number of nuclei fragments contained in epiblast/ectoderm, mesoderm
1106 and hypoblast/endoderm were counted on every section of the E17 (F), E18
1107 (G), E19 (H) and E20 (I) embryos. AM, Amnion; EPI, epiblast; ECT, ectoderm;
1108 ME, mesoderm; HYP, hypoblast; EN, endoderm; YSPE, yolk-sac parietal
1109 endoderm; EXSPM, extraembryonic splanchnic mesoderm; EXSOM,
1110 extraembryonic somatic mesoderm.
1111 J, The percentage of length of primitive streak. The length of embryo was
1112 assessed by total sections, while using sections with gastrulation area to
1113 evaluate the length of primitive streak.
1114 K, Cell numbers and mitotic activity of germ layers of gastrulating monkey
1115 embryos. EPI, epiblast; ECT, ectoderm; ME, mesoderm; HYP, hypoblast; EN,
1116 endoderm.

1117 L. Cell numbers of gastrulation in mouse and primate embryos. The cell number
1118 of primate embryos before E16 were got from in vitro cultured human embryos
1119 (Xiang et al., 2019), and the cell number of primate embryos during gastrulation
1120 were estimated by histological analysis. The cell number of mouse embryos
1121 were adapted from histological determination (Snow, 1977).
1122

1123 Figure S2

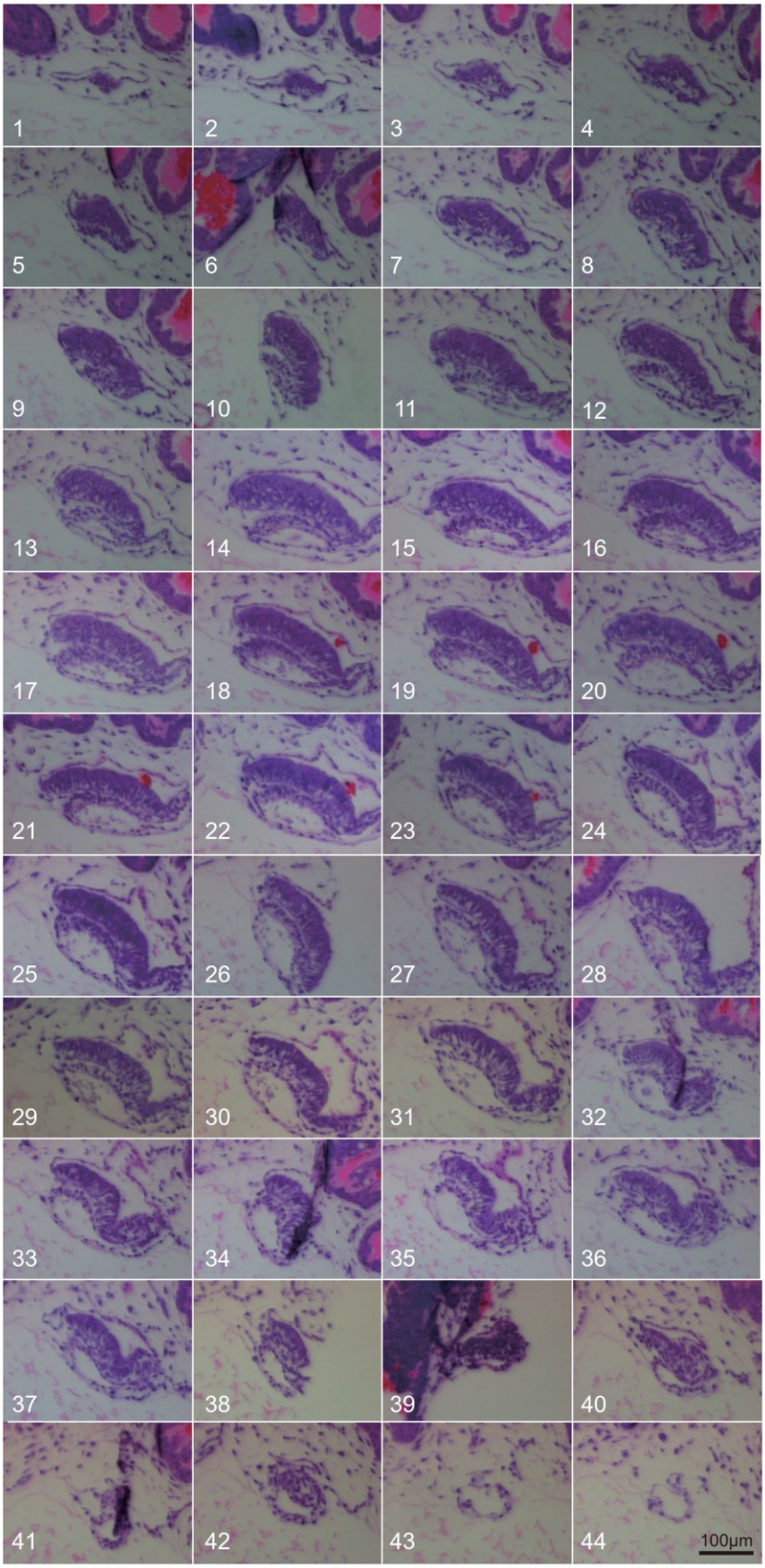

1124

1125 **Figure S2 Histology of serial section of E17 monkey embryo.**

1126 Haematoxylin and eosin staining of the serial sections of gastrulation embryo
1127 at E17. Scale bar, 100μm
1128

1129 Figure S3

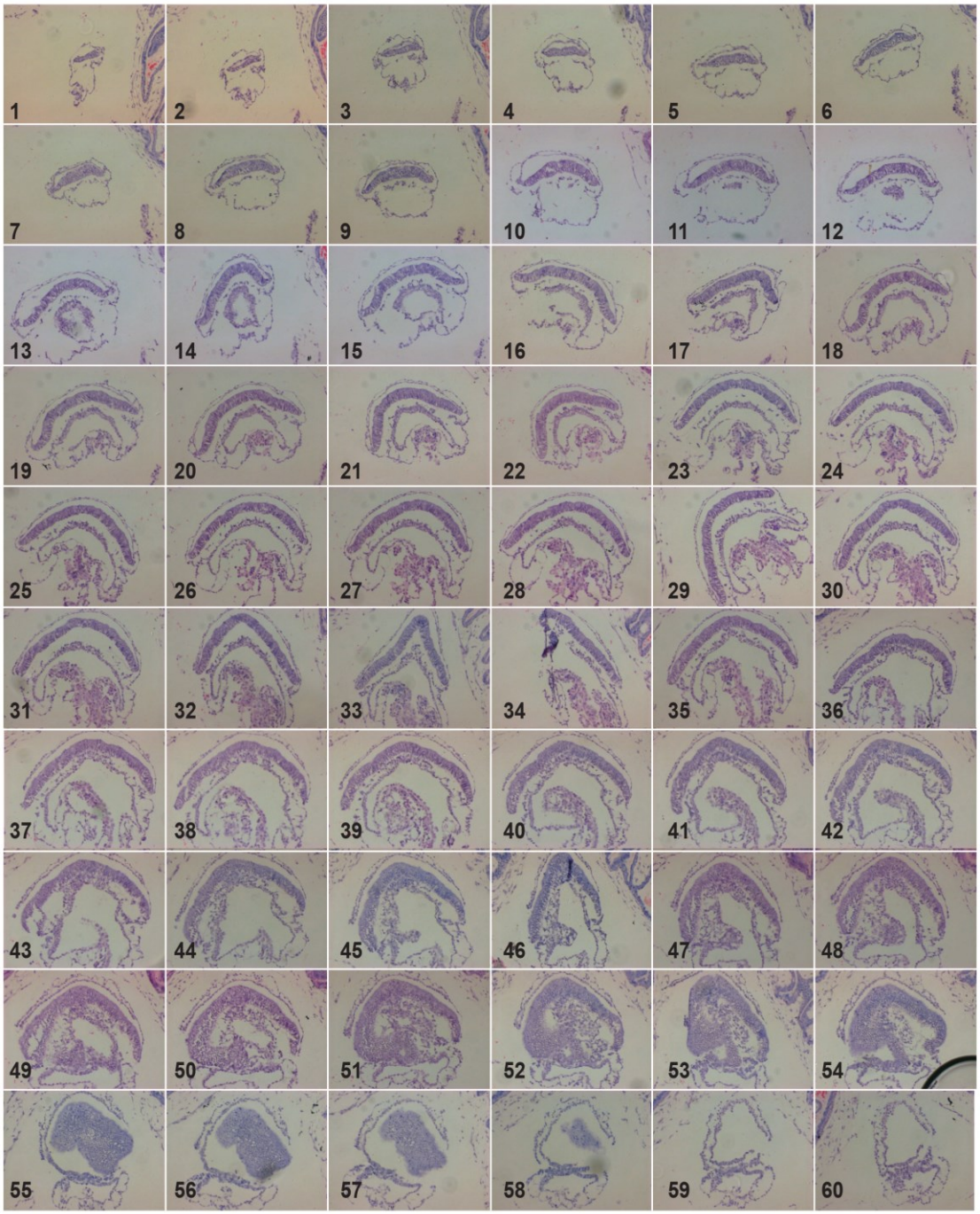

1130

1131 **Figure S3 Histology of serial section of E18 monkey embryo.**

1132 Haematoxylin and eosin staining of the serial sections of gastrulation embryo

1133 at E18. Scale bar, 100μm

1134

Figure S4-PART1

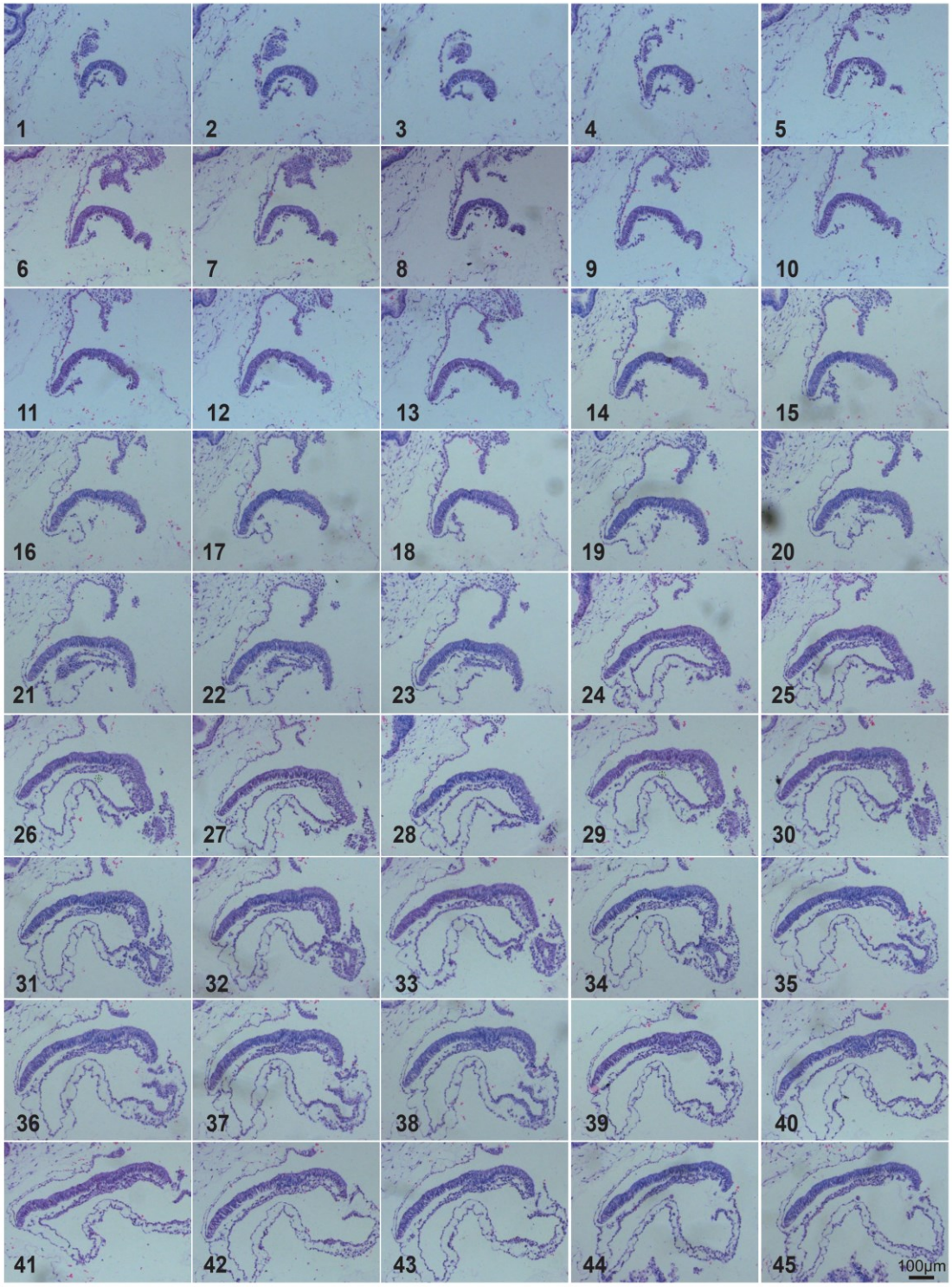

1138 Figure S4-PART2

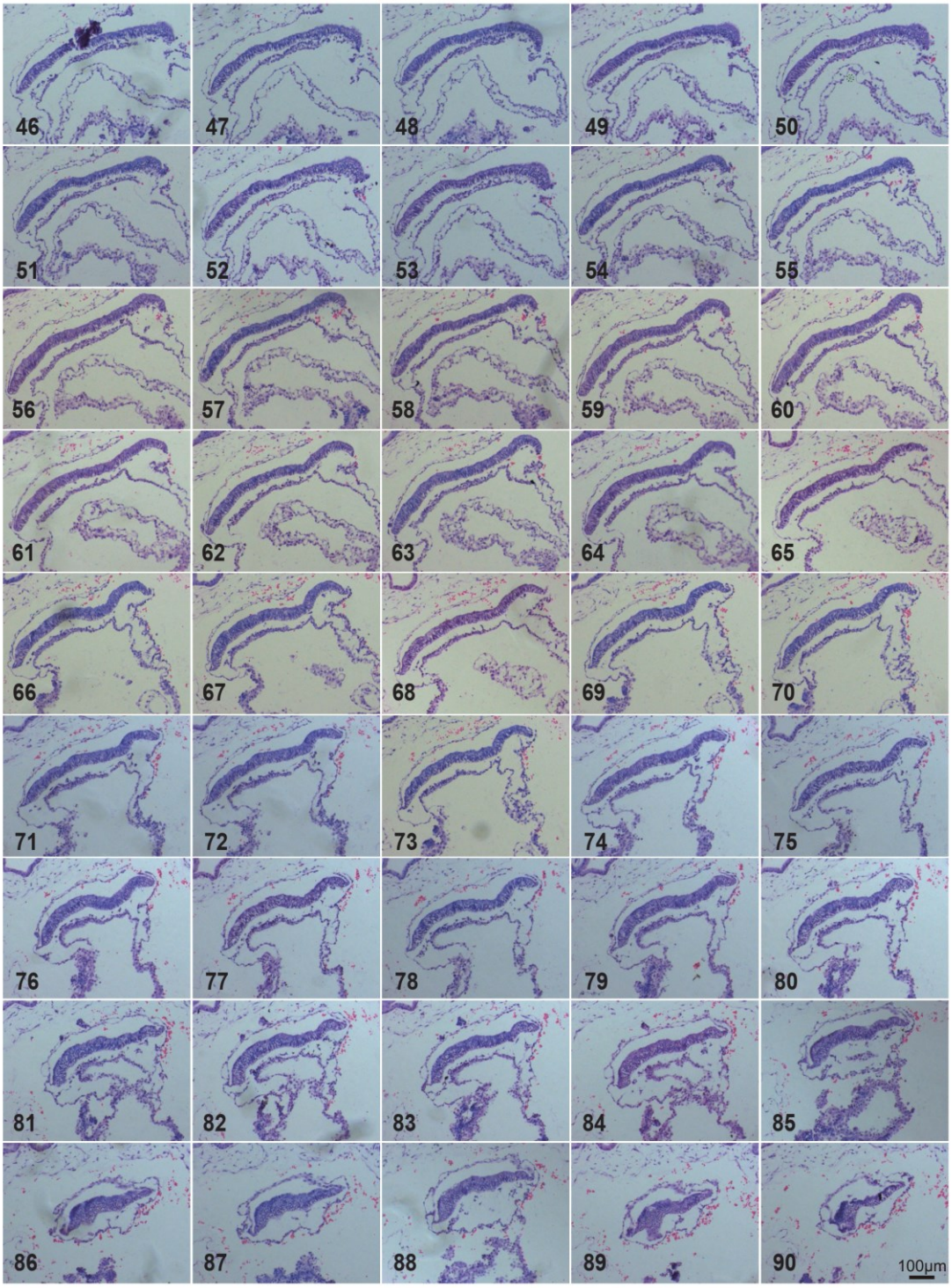

1139

1140 **Figure S4 Histology of serial section of E19 monkey embryo.**

1141 Haematoxylin and eosin staining of the serial sections of gastrulation embryo

1142 at E19. Scale bar, 100μm

Figure S5-PART1

Figure S5-PART2

1149 Figure S5-PART3

1150

1151 **Figure S5 Histology of serial section of E20 monkey embryo.**

1152 Haematoxylin and eosin staining of the serial sections of gastrulation embryo

1153 at E20. Scale bar, 100μm

1154

Figure S6-PART1

1158 Figure S6-PART2

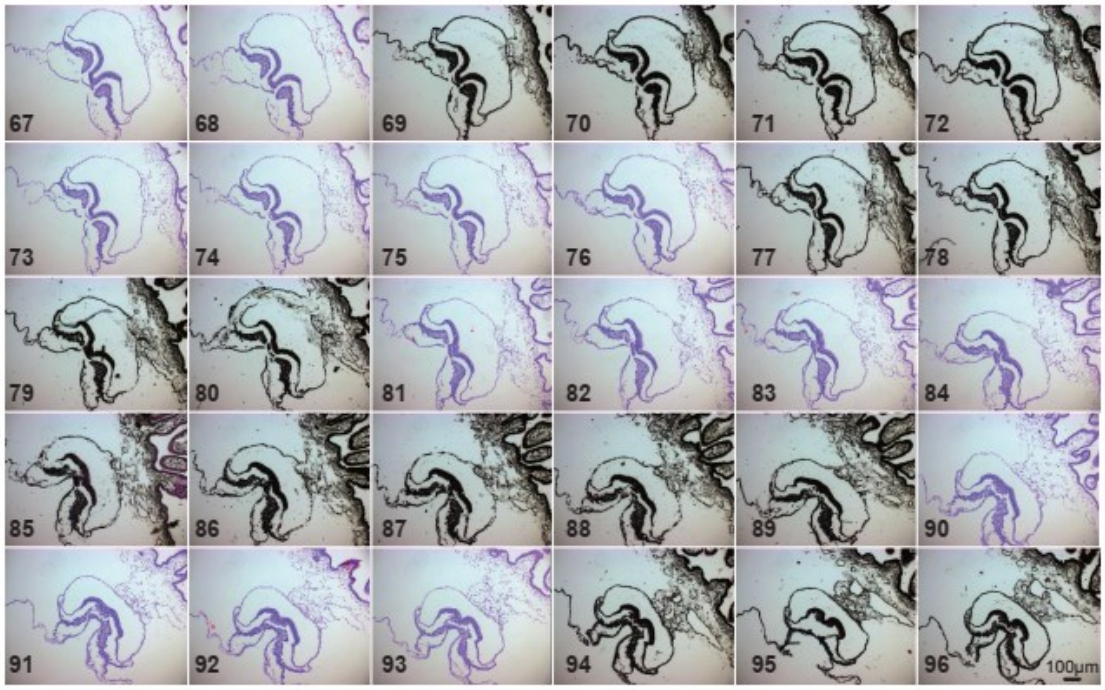

1159

1160 **Figure S6 Histology of serial section of E21 monkey embryo.**

1161 Haematoxylin and eosin staining of the serial sections of gastrulation embryo

1162 at E21. Scale bar, 100μm

1163

Figure S7

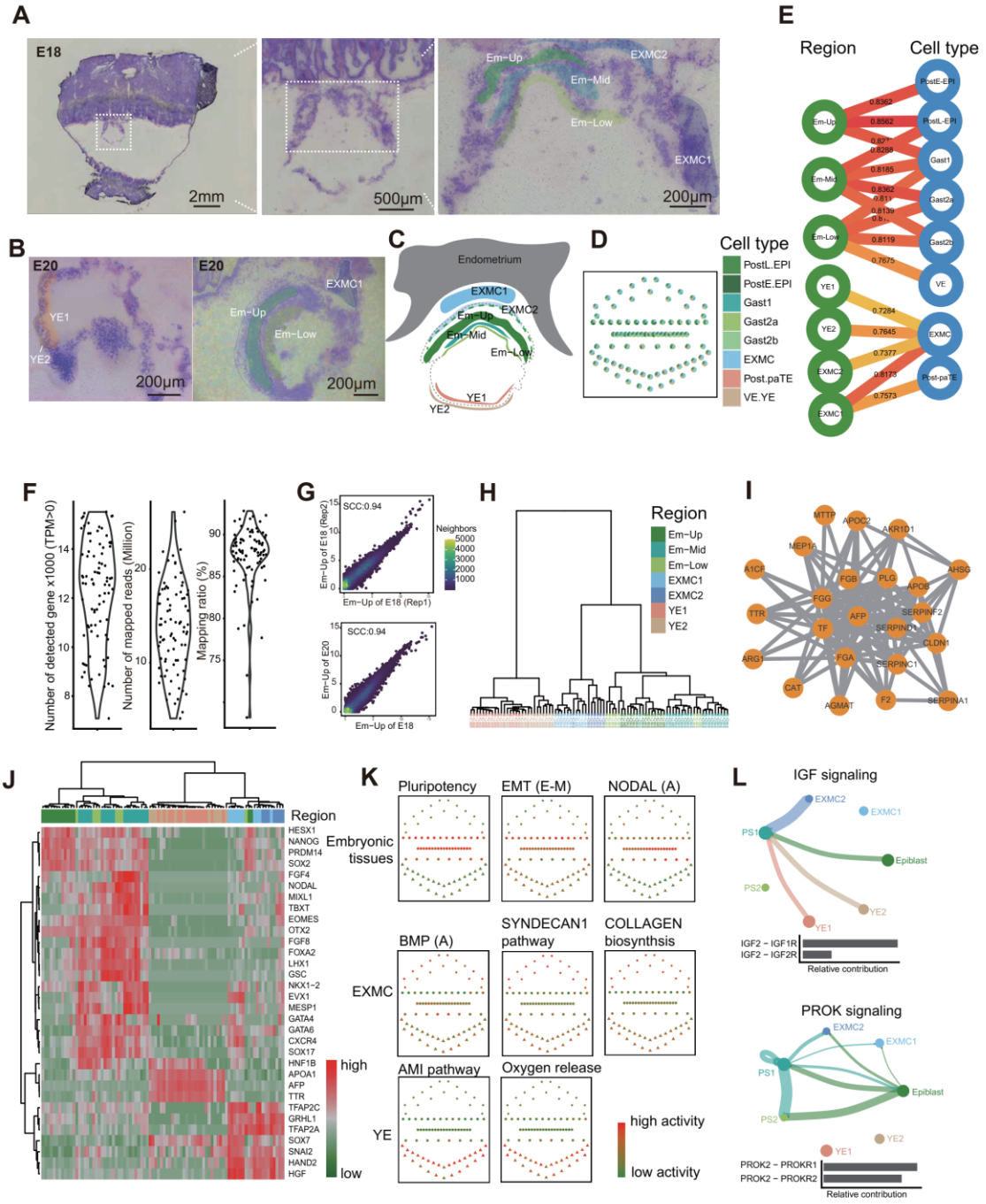
A
E18
2mm
500μm
200μm
Em-Up
EXMC2
Em-Mid
Em-Low
EXMC1
B
E20
YE1
YE2
200μm
C
Endometrium
D
Cell type
PostL.EPI
PostE.EPI
Gast1
Gast2a
Gast2b
EXMC
Post.paTE
VE.YE
E
Region
Cell type
F
Number of detected gene x1000 (TPM>0)
Number of mapped reads (Million)
Mapping ratio (%)
G
SCC:0.94
Neighbors
Em-Up of E18 (Rep1)
Em-Up of E18 (Rep2)
Em-Up of E20
Em-Up of E18
H
Region
Em-Up
Em-Mid
Em-Low
EXMC1
EXMC2
YE1
YE2
I
J
Region
HESX1
NANOG
PRDM14
SOX2
FGF4
NODAL
MIXL1
TBXT
EOMES
OTX2
FGF8
FOXA2
LHX1
GSC
NKX1-2
EVX1
MESP1
GATA4
GATA6
CXCR4
SOX17
HNF1B
APOA1
AFP
TTR
TFAP2C
GRHL1
TFAP2A
SOX7
SNAI2
HAND2
HGF
high
low
K
Pluripotency
EMT (E-M)
NODAL (A)
Embryonic tissues
BMP (A)
SYNDECAN1 pathway
COLLAGEN biosynthsis
EXMC
AMI pathway
Oxygen release
YE
high activity
low activity
L
IGF signaling
EXMC2
EXMC1
PS1
Epiblast
PS2
YE2
YE1
IGF2 - IGF1R
IGF2 - IGF2R
Relative contribution
PROK signaling
PROK2 - PROKR1
PROK2 - PROKR2

1167 **Figure S7 Spatial transcriptome analysis of monkey embryos at E18 and**
1168 **E20 by Geo-seq**

1169 A-C. Embryonic and extraembryonic tissues were captured by laser
1170 microdissection at E18 (A) and E20 (B). Representative sampling locations in
1171 7 different regions were shaded respectively. The schematic diagram showed
1172 the collected tissue regions (C). Em-Up, upper layer of embryonic tissue; Em-
1173 Mid, middle layer of embryonic tissue; Em-Low, lower layer of embryonic tissue;
1174 EXMC1/2, part of extra-embryonic mesenchyme tissues; YE1/2, part of yolk-
1175 sac endoderm.
1176 D. Cell-type deconvolution in spatial transcriptomics samples. The single cell
1177 RNA-seq data of monkey gastrulating embryos was download from previous
1178 work GSE74767 (Nakamura et al., 2016), and the STGE-plot represents the
1179 spatial sampling in monkey embryos. The colour coding is as indicated.
1180 E. The Spearman correlation coefficient of cell population between spatial (red
1181 module) and single cell annotated cell types (blue module, download from
1182 GSE74767 (Nakamura et al., 2016)) showing the location of specific cell. The
1183 color coding is spearman correlation coefficient (SCC).
1184 F. Violin plot showing the number of detected genes (TPM > 0), number of
1185 mapped reads (Million) and mapping ratio of samples (n=86).
1186 G. The Spearman correlation coefficient (SCC) of spatial domain. Upper panel
1187 showed the SCC between embryonic replicates at E18, and lower panel
1188 presented the SCC between developmental stages. The colorbar represent the
1189 density of gene number.
1190 H. Hierarchical clustering analysis for the embryonic and extraembryonic
1191 tissues of monkey embryo based on the expression level of DEGs. Color code
1192 the different sectors.
1193 I. Weighted gene co-expression network analysis (WGCNA) represented as

highest correlation coefficient values for yolk sac endoderm.

J. Heatmap showing the expression pattern of germ-layer marker genes. Top colored bars indicate the sample regions as F.

K. Pathway activity and epithelial-mesenchymal transition (EMT) scores analysis of the embryonic, extra-embryonic mesenchyme and yolk-sac endoderm tissues. The higher EMT scores (E-M), the more epidermal-like state. The colour coding is as indicated.

L. The inferred IGF and PROK signaling networks and relative contribution of each ligand-receptor pair to those overall signaling networks. Circle sizes are proportional to the number of cells in each cell group and edge width represents the communication probability.

Figure S8

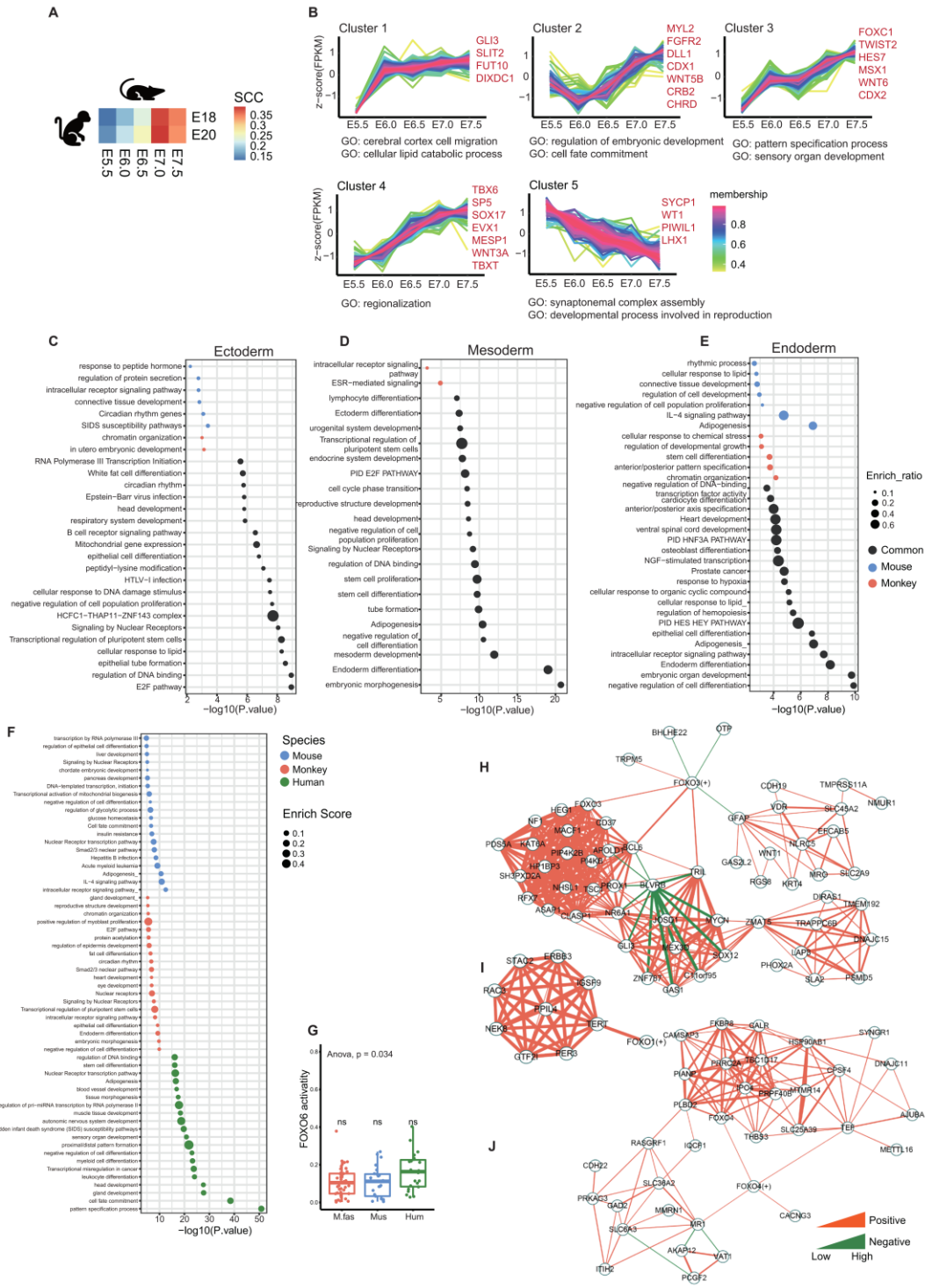
A
SCC
0.35
0.3
0.25
0.2
0.15
E18
E20
E5.5
E6.0
E6.5
E7.0
E7.5
B
Cluster 1
GLI3
SLIT2
FUT10
DIXDC1
GO: cerebral cortex cell migration
GO: cellular lipid catabolic process
Cluster 2
MYL2
FGFR2
DLL1
CDX1
WNT5B
CRB2
CHRD
GO: regulation of embryonic development
GO: cell fate commitment
Cluster 3
FOXC1
TWIST2
HES7
MSX1
WNT6
CDX2
GO: pattern specification process
GO: sensory organ development
Cluster 4
TBX6
SP5
SOX17
EVX1
MESP1
WNT3A
TBXT
GO: regionalization
Cluster 5
SYCP1
WT1
PIWIL1
LHX1
GO: synaptonemal complex assembly
GO: developmental process involved in reproduction
z−score(FPKM)
membership
0.8
0.6
0.4
C
Ectoderm
response to peptide hormone
regulation of protein secretion
intracellular receptor signaling pathway
connective tissue development
Circadian rhythm genes
SIDS susceptibility pathways
chromatin organization
in utero embryonic development
RNA Polymerase III Transcription Initiation
White fat cell differentiation
circadian rhythm
Epstein−Barr virus infection
head development
respiratory system development
B cell receptor signaling pathway
Mitochondrial gene expression
epithelial cell differentiation
peptidyl−lysine modification
HTLV−I infection
cellular response to DNA damage stimulus
negative regulation of cell population proliferation
HCFC1−THAP11−ZNF143 complex
Signaling by Nuclear Receptors
Transcriptional regulation of pluripotent stem cells
cellular response to lipid
epithelial tube formation
regulation of DNA binding
E2F pathway
−log10(P.value)
D
Mesoderm
intracellular receptor signaling pathway
ESR−mediated signaling
lymphocyte differentiation
Ectoderm differentiation
urogenital system development
Transcriptional regulation of pluripotent stem cells
endocrine system development
PID E2F PATHWAY
cell cycle phase transition
reproductive structure development
head development
negative regulation of cell population proliferation
Signaling by Nuclear Receptors
regulation of DNA binding
stem cell proliferation
stem cell differentiation
tube formation
Adipogenesis
negative regulation of cell differentiation
mesoderm development
Endoderm differentiation
embryonic morphogenesis
−log10(P.value)
E
Endoderm
rhythmic process
cellular response to lipid
connective tissue development
regulation of cell development
negative regulation of cell population proliferation
IL−4 signaling pathway
Adipogenesis
cellular response to chemical stress
regulation of developmental growth
stem cell differentiation
anterior/posterior pattern specification
chromatin organization
negative regulation of DNA−binding
transcription factor activity
cardiocyte differentiation
anterior/posterior axis specification
Heart development
ventral spinal cord development
PID HNF3A PATHWAY
osteoblast differentiation
NGF−stimulated transcription
Prostate cancer
response to hypoxia
cellular response to organic cyclic compound
cellular response to lipid
regulation of hemopoiesis
PID HES HEY PATHWAY
epithelial cell differentiation
Adipogenesis
intracellular receptor signaling pathway
Endoderm differentiation
embryonic organ development
negative regulation of cell differentiation
−log10(P.value)
Enrich_ratio
0.1
0.2
0.4
0.6
Common
Mouse
Monkey
F
Species
Mouse
Monkey
Human
Enrich Score
0.1
0.2
0.3
0.4
−log10(P.value)
G
Anova, p = 0.034
FOXO6 activity
ns
ns
ns
M.fas
Mus
Hum
H
I
J
Positive
Negative
Low
High

1208 **Figure S8 Cross-species spatial transcriptomic analysis reveals**
1209 **gastrulation developmental differences among mice, monkeys and**
1210 **humans**

1211 A, Heatmap of Spearman correlation coefficient of expressed gene between
1212 mouse and monkey gastrulating embryos.
1213 B, Cluster analysis of the gene expression patterns across the gastrulation
1214 development stages.
1215 C-E, Dotplot showing functional enrichment of species – specificity regulons in
1216 ectoderm (C), mesoderm (D) and endoderm (E) formation between mouse and
1217 macaque.
1218 F, Functional enrichment, interactome analysis and gene annotation based on
1219 species – specificity regulons.
1220 G, The activities of FOXO6 regulons between mouse, monkey and human
1221 gastrulation embryonic tissue.
1222 H-J, Networks showing the relationship of FOXO1 (H), FOXO3 (I) and FOXO4
1223 (J) with their targets and top 10 related genes, respectively. The color of edges
1224 means positive interaction (orange) or negative interaction (green), and the
1225 width of edges represents the strength of the correlation.
1226
1227

1228 **Table S1. List of the length and thickness of sectioned epiblast from E17**
1229 **to E20, Related to Figure 1**

1230 The gastrulating embryo sizes were assessed by the length and thickness of
1231 sectioned epiblast.

1232 **Table S2. Cell counting of germ layers in gastrulating Cynomolgus**
1233 **monkey embryos, Related to Figure 1**

1234 The detailed histological analysis was applied to determine cell number by
1235 counting nuclei on every section of the gastrulating embryos. The total score
1236 was then adjusted by applying Abercrombie's correction formula to give an
1237 estimate of the actual cell number.

1238 **Table S3. The interspecies differences underlying the germ layer**
1239 **segregation, Related to Figure 7**

1240 The species/spatial domain- specificity score (SSS) of mouse and macaque in
1241 the process of ectoderm, mesoderm and endoderm specification was showed
1242 in sheet 1. The SSS and p-value of interspecies differences in mouse, macaque
1243 and human were listed in sheet 2. The species-specific regulons were listed in
1244 sheet 3.
1245
1246
1247

REFERENCE

Abe, T., Sakaue-Sawano, A., Kiyonari, H., Shioi, G., Inoue, K., Horiuchi, T., Nakao, K., Miyawaki, A., Aizawa, S., and Fujimori, T. (2013). Visualization of cell cycle in mouse embryos with Fucci2 reporter directed by Rosa26 promoter. Development *140*, 237-246.

Abercrombie, M. (1946). Estimation of nuclear population from microtome sections. The Anatomical record *94*, 239-247.

Aibar, S., Gonzalez-Blas, C.B., Moerman, T., Huynh-Thu, V.A., Imrichova, H., Hulselmans, G., Rambow, F., Marine, J.C., Geurts, P., Aerts, J.*, et al.* (2017). SCENIC: single-cell regulatory network inference and clustering. Nature methods.

Andreatta, M., and Carmona, S.J. (2021). UCell: Robust and scalable single-cell gene signature scoring. Computational and structural biotechnology journal *19*, 3796-3798.

Baardman, M.E., Kerstjens-Frederikse, W.S., Berger, R.M., Bakker, M.K., Hofstra, R.M., and Plösch, T. (2013). The role of maternal-fetal cholesterol transport in early fetal life: current insights. Biology of reproduction *88*, 24.

Ben-Haim, N., Lu, C., Guzman-Ayala, M., Pescatore, L., Mesnard, D., Bischofberger, M., Naef, F., Robertson, E.J., and Constam, D.B. (2006). The nodal precursor acting via activin receptors induces mesoderm by maintaining a source of its convertases and BMP4. Developmental cell *11*, 313-323.

Bianchi, D.W., Wilkins-Haug, L.E., Enders, A.C., and Hay, E.D. (1993). Origin of extraembryonic mesoderm in experimental animals: relevance to chorionic mosaicism in humans. American journal of medical genetics *46*, 542-550.

Boroviak, T., Stirparo, G.G., Dietmann, S., Hernando-Herraez, I., Mohammed, H., Reik, W., Smith, A., Sasaki, E., Nichols, J., and Bertone, P. (2018). Single cell transcriptome analysis of human, marmoset and mouse embryos reveals common and divergent features of preimplantation development. Development *145*.

Brennan, J., Lu, C.C., Norris, D.P., Rodriguez, T.A., Beddington, R.S., and Robertson, E.J. (2001). Nodal signalling in the epiblast patterns the early mouse embryo. Nature *411*, 965-969.

Bu, D., Luo, H., Huo, P., Wang, Z., Zhang, S., He, Z., Wu, Y., Zhao, L., Liu, J., Guo, J.*, et al.* (2021). KOBAS-i: intelligent prioritization and exploratory visualization of biological functions for gene enrichment analysis. Nucleic acids research *49*, W317-W325.

Carlson, B.M. (2015). Gastrulation and Germ Layer Formation. In Reference Module in Biomedical Sciences.

Chakraborty, P., George, J.T., Tripathi, S., Levine, H., and Jolly, M.K. (2020). Comparative Study of Transcriptomics-Based Scoring Metrics for the Epithelial-

Hybrid-Mesenchymal Spectrum. Front Bioeng Biotechnol *8*, 220.
Chakravarti, D., LaBella, K.A., and DePinho, R.A. (2021). Telomeres: history, health, and hallmarks of aging. Cell *184*, 306-322.
Chen, J., Suo, S., Tam, P.P., Han, J.J., Peng, G., and Jing, N. (2017). Spatial transcriptomic analysis of cryosectioned tissue samples with Geo-seq. Nature protocols *12*, 566-580.
Chen, S., Zhou, Y., Chen, Y., and Gu, J. (2018). fastp: an ultra-fast all-in-one FASTQ preprocessor. Bioinformatics *34*, i884-i890.
Chhabra, S., Liu, L., Goh, R., Kong, X., and Warmflash, A. (2019). Dissecting the dynamics of signaling events in the BMP, WNT, and NODAL cascade during self-organized fate patterning in human gastruloids. PLoS biology *17*, e3000498.
Cindrova-Davies, T., Jauniaux, E., Elliot, M.G., Gong, S., Burton, G.J., and Charnock-Jones, D.S. (2017). RNA-seq reveals conservation of function among the yolk sacs of human, mouse, and chicken. Proceedings of the National Academy of Sciences of the United States of America *114*, E4753-E4761.
Ciruna, B., and Rossant, J. (2001). FGF Signaling Regulates Mesoderm Cell Fate Specification and Morphogenetic Movement at the Primitive Streak. Developmental cell *1*, 37-49.
Cui, G., Chen, J., Chen, S., Qian, Y., Peng, G., and Jing, N. (2019). Spatio-temporal transcriptome construction of early mouse embryo with Geo-seq and Auto-seq. Protocol Exchange, 10.21203/rs.21202.10081/v21201.
de Bakker, B.S., de Jong, K.H., Hagoort, J., de Bree, K., Besselink, C.T., de Kanter, F.E.C., Veldhuis, T., Bais, B., Schildmeijer, R., Ruijter, J.M.*, et al.* (2016). An interactive three-dimensional digital atlas and quantitative database of human development. Science *354*, aag0053.
DeTomaso, D., Jones, M.G., Subramaniam, M., Ashuach, T., Ye, C.J., and Yosef, N. (2019). Functional interpretation of single cell similarity maps. Nature communications *10*, 4376.
Dong, D., and Yang, P. (2018). Yolk Sac. In Encyclopedia of Reproduction (Second Edition), M.K. Skinner, ed. (Oxford: Academic Press), pp. 551-558.
Dongre, A., and Weinberg, R.A. (2019). New insights into the mechanisms of epithelial-mesenchymal transition and implications for cancer. Nature reviews Molecular cell biology *20*, 69-84.
Drost, H.-G. (2018). Philentropy: Information Theory and Distance Quantification with R. Journal of Open Source Software *3*.
Dufort, D., Schwartz, L., Harpal, K., and Rossant, J. (1998). The transcription factor HNF3beta is required in visceral endoderm for normal primitive streak morphogenesis. Development *125*, 3015-3025.
Eivers, E., McCarthy, K., Glynn, C., Nolan, C.M., and Byrnes, L. (2004). Insulin-like growth factor (IGF) signalling is required for early dorso-anterior

development of the zebrafish embryo. The International journal of developmental biology *48*, 1131-1140.
Elosua-Bayes, M., Nieto, P., Mereu, E., Gut, I., and Heyn, H. (2021). SPOTlight: seeded NMF regression to deconvolute spatial transcriptomics spots with single-cell transcriptomes. Nucleic acids research.
Enders, A.C., and King, B.F. (1988). Formation and differentiation of extraembryonic mesoderm in the rhesus monkey. The American journal of anatomy *181*, 327-340.
Enders, A.C., Schlafke, S., and Hendrickx, A.G. (1986). Differentiation of the embryonic disc, amnion, and yolk sac in the rhesus monkey. The American journal of anatomy *177*, 161-185.
Exalto, N. (1995). Early human nutrition. European Journal of Obstetrics & Gynecology and Reproductive Biology *61*, 3-6.
Feng, S., Xing, C., Shen, T., Qiao, Y., Wang, R., Chen, J., Liao, J., Lu, Z., Yang, X., Abd-Allah, S.M.*, et al.* (2017). Abnormal Paraventricular Nucleus of Hypothalamus and Growth Retardation Associated with Loss of Nuclear Receptor Gene COUP-TFII. Scientific reports *7*, 5282.
Fu, J., Warmflash, A., and Lutolf, M.P. (2020). Stem-cell-based embryo models for fundamental research and translation. Nature materials.
Gao, Y., Cao, Q., Lu, L., Zhang, X., Zhang, Z., Dong, X., Jia, W., and Cao, Y. (2015). Kruppel-like factor family genes are expressed during Xenopus embryogenesis and involved in germ layer formation and body axis patterning. *244*, 1328-1346.
Ghimire, S., Mantziou, V., Moris, N., and Arias, A.M. (2021). Human gastrulation: The embryo and its models. Developmental biology.
Grapin-Botton, A., and Constam, D. (2007). Evolution of the mechanisms and molecular control of endoderm formation. Mechanisms of development *124*, 253-278.
Grobstein, C. (1985). The early development of human embryos. The Journal of medicine and philosophy *10*, 213-236.
Gualdi, R., Bossard, P., Zheng, M., Hamada, Y., Coleman, J.R., and Zaret, K.S. (1996). Hepatic specification of the gut endoderm in vitro: cell signaling and transcriptional control. Genes & development *10*, 1670-1682.
Hannenhalli, S., and Kaestner, K.H. (2009). The evolution of Fox genes and their role in development and disease. Nature reviews Genetics *10*, 233-240.
Hendrickx, A.G. (1972). Early development of the embryo in non-human primates and man. Acta endocrinologica Supplementum *166*, 103-130.
Hyun, I., Bredenoord, A.L., Briscoe, J., Klipstein, S., and Tan, T. (2021). Human embryo research beyond the primitive streak. Science *371*, 998-1000.
Jin, S., Guerrero-Juarez, C.F., Zhang, L., Chang, I., Ramos, R., Kuan, C.H., Myung, P., Plikus, M.V., and Nie, Q. (2021). Inference and analysis of cell-cell communication using CellChat. Nature communications *12*, 1088.

Kaestner, K.H., Hiemisch, H., and Schütz, G. (1998). Targeted disruption of the gene encoding hepatocyte nuclear factor 3gamma results in reduced transcription of hepatocyte-specific genes. Molecular and cellular biology *18*, 4245-4251.

Lai, E., Prezioso, V.R., Tao, W.F., Chen, W.S., and Darnell, J.E., Jr. (1991). Hepatocyte nuclear factor 3 alpha belongs to a gene family in mammals that is homologous to the Drosophila homeotic gene fork head. Genes & development *5*, 416-427.

Lamouille, S., Xu, J., and Derynck, R. (2014). Molecular mechanisms of epithelial-mesenchymal transition. Nature reviews Molecular cell biology *15*, 178-196.

Langfelder, P., and Horvath, S. (2008). WGCNA: an R package for weighted correlation network analysis. BMC bioinformatics *9*, 559.

Larsson, L., Frisen, J., and Lundeberg, J. (2021). Spatially resolved transcriptomics adds a new dimension to genomics. Nature methods *18*, 15-18.

Lawson, K.A., and Wilson, V. (2016). A Revised Staging of Mouse Development Before Organogenesis. In Kaufman's Atlas of Mouse Development Supplement, pp. 51-64.

Luckett, W.P. (1978). Origin and differentiation of the yolk sac and extraembryonic mesoderm in presomite human and rhesus monkey embryos. The American journal of anatomy *152*, 59-97.

Ma, H., Zhai, J., Wan, H., Jiang, X., Wang, X., Wang, L., Xiang, Y., He, X., Zhao, Z.A., Zhao, B.*, et al.* (2019). In vitro culture of Cynomolgus monkey embryos beyond early gastrulation. Science *366*.

Massri, A.J., Schiebinger, G.R., Berrio, A., Wang, L., Wray, G.A., and McClay, D.R. (2021). The Epithelialto Mesenchymal Transition. Methods Mol Biol *2179*, 303-314.

McDole, K., Guignard, L., Amat, F., Berger, A., Malandain, G., Royer, L.A., Turaga, S.C., Branson, K., and Keller, P.J. (2018). In Toto Imaging and Reconstruction of Post-Implantation Mouse Development at the Single-Cell Level. Cell.

Mengjun, L.G. (2019). TCseq: Time course sequencing data analysis.

Mitiku, N., and Baker, J.C. (2007). Genomic analysis of gastrulation and organogenesis in the mouse. Developmental cell *13*, 897-907.

Mittnenzweig, M., Mayshar, Y., Cheng, S., Ben-Yair, R., Hadas, R., Rais, Y., Chomsky, E., Reines, N., Uzonyi, A., Lumerman, L.*, et al.* (2021). A single-embryo, single-cell time-resolved model for mouse gastrulation. Cell.

Monaghan, A.P., Kaestner, K.H., Grau, E., and Schütz, G. (1993). Postimplantation expression patterns indicate a role for the mouse forkhead/HNF-3 alpha, beta and gamma genes in determination of the definitive endoderm, chordamesoderm and neuroectoderm. Development *119*, 567-578.

Moore, H.D., Gems, S., and Hearn, J.P. (1985). Early implantation stages in the

marmoset monkey (Callithrix jacchus). The American journal of anatomy *172*, 265-278.
Moris, N., Anlas, K., van den Brink, S.C., Alemany, A., Schröder, J., Ghimire, S., Balayo, T., van Oudenaarden, A., and Martinez Arias, A. (2020). An in vitro model of early anteroposterior organization during human development. Nature *582*, 410-415.
Muller, F., and O'Rahilly, R. (2004). The primitive streak, the caudal eminence and related structures in staged human embryos. Cells, tissues, organs *177*, 2-20.
Nakamura, T., Fujiwara, K., Saitou, M., and Tsukiyama, T. (2021). Non-human primates as a model for human development. Stem Cell Reports *16*, 1093-1103.
Nakamura, T., Okamoto, I., Sasaki, K., Yabuta, Y., Iwatani, C., Tsuchiya, H., Seita, Y., Nakamura, S., Yamamoto, T., and Saitou, M. (2016). A developmental coordinate of pluripotency among mice, monkeys and humans. Nature *537*, 57-62.
Nicetto, D., Donahue, G., Jain, T., Peng, T., Sidoli, S., Sheng, L., Montavon, T., Becker, J.S., Grindheim, J.M., Blahnik, K.*, et al.* (2019). H3K9me3-heterochromatin loss at protein-coding genes enables developmental lineage specification. *363*, 294-297.
Nikolopoulou, E., Galea, G.L., Rolo, A., Greene, N.D., and Copp, A.J. (2017). Neural tube closure: cellular, molecular and biomechanical mechanisms. Development *144*, 552-566.
Niu, Y., Sun, N., Li, C., Lei, Y., Huang, Z., Wu, J., Si, C., Dai, X., Liu, C., Wei, J.*, et al.* (2019). Dissecting primate early post-implantation development using long-term in vitro embryo culture. Science *366*, 5754.
Nowotschin, S., Hadjantonakis, A.K., and Campbell, K. (2019). The endoderm: a divergent cell lineage with many commonalities. Development *146*, dev150920.
O'Rahilly, R., and Muller, F. (2010). Developmental stages in human embryos: revised and new measurements. Cells, tissues, organs *192*, 73-84.
Otasek, D., Morris, J.H., Boucas, J., Pico, A.R., and Demchak, B. (2019). Cytoscape Automation: empowering workflow-based network analysis. Genome biology *20*, 185.
Peng, G., Cui, G., Ke, J., and Jing, N. (2020a). Using Single-Cell and Spatial Transcriptomes to Understand Stem Cell Lineage Specification During Early Embryo Development. Annual Review of Genomics and Human Genetics *21*, 163-181.
Peng, G., Cui, G., Ke, J., and Jing, N. (2020b). Using Single-Cell and Spatial Transcriptomes to Understand Stem Cell Lineage Specification During Early Embryo Development. Annu Rev Genomics Hum Genet *21*, 163-181.
Peng, G., Suo, S., Chen, J., Chen, W., Liu, C., Yu, F., Wang, R., Chen, S., Sun, N., Cui, G.*, et al.* (2016). Spatial Transcriptome for the Molecular Annotation of

Lineage Fates and Cell Identity in Mid-gastrula Mouse Embryo. Developmental cell *36*, 681-697.
Peng, G., Suo, S., Cui, G., Yu, F., Wang, R., Chen, J., Chen, S., Liu, Z., Chen, G., Qian, Y.*, et al.* (2019). Molecular architecture of lineage allocation and tissue organization in early mouse embryo. Nature *572*, 528-532.
Peng, H., Ruan, Z., Long, F., Simpson, J.H., and Myers, E.W. (2010). V3D enables real-time 3D visualization and quantitative analysis of large-scale biological image data sets. Nat Biotechnol *28*, 348-353.
Pertea, M., Kim, D., Pertea, G.M., Leek, J.T., and Salzberg, S.L. (2016). Transcript-level expression analysis of RNA-seq experiments with HISAT, StringTie and Ballgown. Nature protocols *11*, 1650-1667.
Pfister, S., Steiner, K.A., and Tam, P.P. (2007). Gene expression pattern and progression of embryogenesis in the immediate post-implantation period of mouse development. Gene expression patterns : GEP *7*, 558-573.
Pijuan-Sala, B., Guibentif, C., and Gottgens, B. (2018). Single-cell transcriptional profiling: a window into embryonic cell-type specification. Nature reviews Molecular cell biology.
Rivera-Perez, J.A., and Hadjantonakis, A.K. (2015). The Dynamics of Morphogenesis in the Early Mouse Embryo. Cold Spring Harb Perspect Biol *7*.
Rivera-Perez, J.A., and Magnuson, T. (2005). Primitive streak formation in mice is preceded by localized activation of Brachyury and Wnt3. Developmental biology *288*, 363-371.
Ross, C., and Boroviak, T.E. (2020). Origin and function of the yolk sac in primate embryogenesis. Nature communications *11*, 3760.
Sasaki, H., and Hogan, B.L. (1993). Differential expression of multiple fork head related genes during gastrulation and axial pattern formation in the mouse embryo. Development *118*, 47-59.
Scheibner, K., Schirge, S., Burtscher, I., Buttner, M., Sterr, M., Yang, D., Bottcher, A., Ansarullah, Irmler, M., Beckers, J.*, et al.* (2021). Epithelial cell plasticity drives endoderm formation during gastrulation. Nat Cell Biol.
Schindelin, J., Arganda-Carreras, I., Frise, E., Kaynig, V., Longair, M., Pietzsch, T., Preibisch, S., Rueden, C., Saalfeld, S., Schmid, B.*, et al.* (2012). Fiji: an open-source platform for biological-image analysis. Nature methods *9*, 676-682.
Shahbazi, M.N. (2020). Mechanisms of human embryo development: from cell fate to tissue shape and back. Development *147*, dev190629.
Sheaffer, K.L., and Kaestner, K.H. (2012). Transcriptional networks in liver and intestinal development. Cold Spring Harb Perspect Biol *4*, a008284.
Singh, M., Yelle, N., Venugopal, C., and Singh, S.K. (2018). EMT: Mechanisms and therapeutic implications. Pharmacol Ther *182*, 80-94.
Snow, M. (1977). Gastrulation in the mouse: growth and regionalization of the epiblast. Journal of embryology and experimental morphology *42*, 293-303.
Souilhol, C., Perea-Gomez, A., Camus, A., Beck-Cormier, S., Vandormael-

Pournin, S., Escande, M., Collignon, J., and Cohen-Tannoudji, M. (2015). NOTCH activation interferes with cell fate specification in the gastrulating mouse embryo. Development *142*, 3649-3660.

Stuart, T., Butler, A., Hoffman, P., Hafemeister, C., Papalexi, E., Mauck, W.M., 3rd, Hao, Y., Stoeckius, M., Smibert, P., and Satija, R. (2019). Comprehensive Integration of Single-Cell Data. Cell *177*, 1888-1902 e1821.

Sun, X., Meyers, E.N., Lewandoski, M., and Martin, G.R. (1999). Targeted disruption of Fgf8 causes failure of cell migration in the gastrulating mouse embryo. Genes & development *13*, 1834-1846.

Suo, S., Zhu, Q., Saadatpour, A., Fei, L., Guo, G., and Yuan, G.C. (2018). Revealing the Critical Regulators of Cell Identity in the Mouse Cell Atlas. Cell Rep *25*, 1436-1445 e1433.

Tam, P.P., and Behringer, R.R. (1997). Mouse gastrulation: the formation of a mammalian body plan. Mechanisms of development *68*, 3-25.

Tam, P.P.L., and Ho, J.W.K. (2020). Cellular diversity and lineage trajectory: insights from mouse single cell transcriptomes. Development *147*.

Tang, T.T.-L., Dowbenko, D., Jackson, A., Toney, L., Lewin, D.A., Dent, A.L., and Lasky, L.A. (2002). The Forkhead Transcription Factor AFX Activates Apoptosis by Induction of the BCL-6 Transcriptional Repressor *. Journal of Biological Chemistry *277*, 14255-14265.

Tani, S., Chung, U.I., Ohba, S., and Hojo, H. (2020). Understanding paraxial mesoderm development and sclerotome specification for skeletal repair. Exp Mol Med.

Tarara, R., Enders, A.C., Hendrickx, A.G., Gulamhusein, N., Hodges, J.K., Hearn, J.P., Eley, R.B., and Else, J.G. (1987). Early implantation and embryonic development of the baboon: stages 5, 6 and 7. Anat Embryol (Berl) *176*, 267-275.

Thieme, R., Ramin, N., Fischer, S., Puschel, B., Fischer, B., and Santos, A.N. (2012). Gastrulation in rabbit blastocysts depends on insulin and insulin-like-growth-factor 1. Molecular and cellular endocrinology *348*, 112-119.

Tyser, R.C.V., Mahammadov, E., Nakanoh, S., Vallier, L., Scialdone, A., and Srinivas, S. (2020). A spatially resolved single cell atlas of human gastrulation.

Tyser, R.C.V., Mahammadov, E., Nakanoh, S., Vallier, L., Scialdone, A., and Srinivas, S. (2021). Single-cell transcriptomic characterization of a gastrulating human embryo. Nature.

Varelas, X., Sakuma, R., Samavarchi-Tehrani, P., Peerani, R., Rao, B.M., Dembowy, J., Yaffe, M.B., Zandstra, P.W., and Wrana, J.L. (2008). TAZ controls Smad nucleocytoplasmic shuttling and regulates human embryonic stem-cell self-renewal. Nat Cell Biol *10*, 837-848.

Viotti, M., Nowotschin, S., and Hadjantonakis, A.K. (2014). SOX17 links gut endoderm morphogenesis and germ layer segregation. Nat Cell Biol *16*, 1146-1156.

Wang, C., Liu, X., Gao, Y., Yang, L., Li, C., Liu, W., Chen, C., Kou, X., Zhao, Y., Chen, J., *et al.* (2018). Reprogramming of H3K9me3-dependent heterochromatin during mammalian embryo development. Nat Cell Biol *20*, 620-631.

Wong, E.A., and Uni, Z. (2021). Centennial Review: The chicken yolk sac is a multifunctional organ. Poult Sci *100*, 100821.

Xiang, L., Yin, Y., Zheng, Y., Ma, Y., Li, Y., Zhao, Z., Guo, J., Ai, Z., Niu, Y., Duan, K., *et al.* (2019). A developmental landscape of 3D-cultured human pre-gastrulation embryos. Nature *577*, 537-542.

Yamasaki, J., Iwatani, C., Tsuchiya, H., Okahara, J., Sankai, T., and Torii, R. (2011). Vitrification and transfer of Cynomolgus monkey (Macaca fascicularis) embryos fertilized by intracytoplasmic sperm injection. Theriogenology *76*, 33-38.

Yamashita, S., Ogawa, K., Ikei, T., Fujiki, T., and Katakura, Y. (2014). FOXO3a potentiates hTERT gene expression by activating c-MYC and extends the replicative life-span of human fibroblast. PloS one *9*, e101864.

Yang, J., Wang, B., Chen, H., Chen, X., Li, J., Chen, Y., Yuan, D., and Zheng, S. (2019). Thyrotroph embryonic factor is downregulated in bladder cancer and suppresses proliferation and tumorigenesis via the AKT/FOXOs signalling pathway. Cell Prolif *52*, e12560.

Yang, R., Goedel, A., Kang, Y., Si, C., Chu, C., Zheng, Y., Chen, Z., Gruber, P.J., Xiao, Y., Zhou, C., *et al.* (2021). Amnion signals are essential for mesoderm formation in primates. Nature communications *12*, 5126.

Yeung, T.L., Leung, C.S., Wong, K.K., Gutierrez-Hartmann, A., Kwong, J., Gershenson, D.M., and Mok, S.C. (2017). ELF3 is a negative regulator of epithelial-mesenchymal transition in ovarian cancer cells. Oncotarget *8*, 16951-16963.

Yu, G., Wang, L.G., Han, Y., and He, Q.Y. (2012). clusterProfiler: an R package for comparing biological themes among gene clusters. OMICS *16*, 284-287.

Zhang, X., Yalcin, S., Lee, D.F., Yeh, T.Y., Lee, S.M., Su, J., Mungamuri, S.K., Rimmele, P., Kennedy, M., Sellers, R., *et al.* (2011). FOXO1 is an essential regulator of pluripotency in human embryonic stem cells. Nat Cell Biol *13*, 1092-1099.

Zhang, Y., Ma, Y., Huang, Y., Zhang, Y., Jiang, Q., Zhou, M., and Su, J. (2020). Benchmarking algorithms for pathway activity transformation of single-cell RNA-seq data. Computational and structural biotechnology journal *18*, 2953-2961.

Zheng, Y., Xue, X., Shao, Y., Wang, S., Esfahani, S.N., Li, Z., Muncie, J.M., Lakins, J.N., Weaver, V.M., Gumucio, D.L., *et al.* (2019). Controlled modelling of human epiblast and amnion development using stem cells. Nature *573*, 421-425.

Zhou, Y., Zhou, B., Pache, L., Chang, M., Khodabakhshi, A.H., Tanaseichuk, O.,

1582 Benner, C., and Chanda, S.K. (2019). Metascape provides a biologist-oriented
1583 resource for the analysis of systems-level datasets. Nature communications *10*,
1584 1523.
1585